Key Points:
- WACCM6 is a major upgrade to previous versions
- WACCM6 can reproduce many modes of variability and trends in the middle atmosphere
- WACCM6 provides improvements in high-latitude climate variability at the surface and sea ice extent over a low top model

Correspondence to:
A Gettelman,
andrew@ucar.edu

Author Contributions
Data curation: M. J. Mills, D. R. Marsh
Software: M. J. Mills, F. Vitt
Formal Analysis: D. E. Kinnison, R. R. Garcia, A. K. Smith, D. R. Marsh, S. Tilmes, C. G. Bardeen, L. K. Emmons, J. H. Richter, A. S. Glanville, A. S. Phillips, R. B. Neale, I. R. Simpson, A. K. DuVivier, W. J. Randel
Investigation: D. R. Marsh, L. K. Emmons, A. S. Glanville, A. S. Phillips, R. B. Neale, I. R. Simpson, A. K. DuVivier, W. J. Randel
Project Administration: R. R. Garcia
Supervision: L. M. Polvani
Writing - review & editing: M. J. Mills, D. E. Kinnison, R. R. Garcia, A. K. Smith, S. Tilmes, C. G. Bardeen, H.-L. Liu, S. C. Solomon, L. M. Polvani, L. K. Emmons, J.-F. Lamarque, J. H. Richter, A. S. Glanville, J. T. Bacmeister, A. S. Phillips, R. B. Neale, I. R. Simpson, A. K. DuVivier, A. Hodzic, W. J. Randel

The Whole Atmosphere Community Climate Model Version 6 (WACCM6)

A. Gettelman[1], M. J. Mills[1], D. E. Kinnison[1], R. R. Garcia[1], A. K. Smith[1], D. R. Marsh[1,2], S. Tilmes[1], F. Vitt[1], C. G. Bardeen[1], J. McInerny[1], H.-L. Liu[1], S. C. Solomon[1], L. M. Polvani[3], L. K. Emmons[1], J.-F. Lamarque[1], J. H. Richter[1], A. S. Glanville[1], J. T. Bacmeister[1], A. S. Phillips[1], R. B. Neale[1], I. R. Simpson[1], A. K. DuVivier[1], A. Hodzic[1], and W. J. Randel[1]

[1]National Center for Atmospheric Research, Boulder, CO, USA, [2]School of Earth and Environment, University of Leeds, Leeds, UK, [3]Department of Applied Mathematics, Columbia University, New York, NY, USA

Abstract The Whole Atmosphere Community Climate Model version 6 (WACCM6) is a major update of the whole atmosphere modeling capability in the Community Earth System Model (CESM), featuring enhanced physical, chemical and aerosol parameterizations. This work describes WACCM6 and some of the important features of the model. WACCM6 can reproduce many modes of variability and trends in the middle atmosphere, including the quasi-biennial oscillation, stratospheric sudden warmings, and the evolution of Southern Hemisphere springtime ozone depletion over the twentieth century. WACCM6 can also reproduce the climate and temperature trends of the 20th century throughout the atmospheric column. The representation of the climate has improved in WACCM6, relative to WACCM4. In addition, there are improvements in high-latitude climate variability at the surface and sea ice extent in WACCM6 over the lower top version of the model (CAM6) that comes from the extended vertical domain and expanded aerosol chemistry in WACCM6, highlighting the importance of the stratosphere and tropospheric chemistry for high-latitude climate variability.

Plain Language Summary This manuscript describes the Whole Atmosphere Community Climate Model Version 6 (WACCM6), a chemistry and climate model which extends up to 140 km in the upper atmosphere. WACCM6 reproduces many important features of the climate system, and the addition of detailed chemistry and the higher than normal model top produces slightly improved simulations of the Arctic region.

1. Introduction

The climate system is driven by energy from the Sun, mediated by the absorption and scattering of that energy by the atmosphere (including clouds) before it arrives at the surface of the Earth. Simulating the climate system means more than just simulation of the surface climate and the troposphere. For example, the climate and chemistry of the stratosphere may also affect the surface, by changing surface forcing through the climatology of water vapor and ozone (Solomon et al., 2010), by stratospheric aerosol loading (Mills et al., 2016), or dynamical interactions between the stratosphere and troposphere with impacts all the way to the surface (Baldwin & Dunkerton, 2001). Thompson et al. (2002) and Charlton-Perez et al. (2013) illustrated how the middle atmosphere can improve predictability of the lower atmosphere. In addition to surface climate variables such as temperature and precipitation, the climate system includes chemical reactions that impact humans and ecosystems through the oxidizing capacity of the troposphere, including near-surface and tropospheric ozone (e.g., Lefohn et al., 2018). Changes in chemistry and dynamics also affect absorbed radiation through the stratospheric ozone layer (World Meteorological Organization, 2011). Stratospheric ozone changes are the premier example of the influence of stratospheric composition on climate (e.g., Son et al., 2010) and air quality (Hodzic & Madronich, 2018). Finally, the dynamics of the sun may affect the atmosphere, particularly the upper atmosphere (from the mesosphere to thermosphere to ionosphere). In periods of extreme solar activity, solar forcing, mediated by upper atmospheric processes, can impact electrically sensitive human structures from power grids to electronic devices, making it critical to understand the "whole" atmosphere.

Simulating the Earth system and its impacts on human health and ecosystems requires the use of comprehensive simulations that can represent the physical, dynamical, and chemical climate of the whole atmosphere. It is for precisely this reason that the Whole Atmosphere Community Climate Model (WACCM) was developed (Garcia et al., 2007) and also used for coupled climate simulations (Marsh et al., 2013).

WACCM was developed for, and has been used to examine many important science questions that can only be addressed with whole atmosphere models. Prior studies with WACCM include trends resulting from increasing greenhouse gases (e.g., Garcia et al., 2007), the climatology of the tropical tropopause layer (Gettelman & Birner, 2007), the response of the atmosphere to the solar cycle and the flux of energetic particles (e.g., Jackman et al., 2009; Marsh et al., 2007; Matthes et al., 2010), the development and recovery of the ozone hole (Eyring et al., 2007, 2010), the response of the stratosphere to El Niño–Southern Oscillation (Calvo et al., 2010; Sassi et al., 2004), and to understand effects of stratospheric geoengineering (Tilmes et al., 2009). WACCM has also been run as the atmosphere in an Earth system model coupled to an ocean (Marsh et al., 2013) and that version (WACCM4) has been used to study the impact of volcanic eruptions on tropospheric climate (Mills et al., 2017), stratospheric temperature trends (Randel et al., 2017), and the processes driving the quasi-biennial oscillation (Garcia & Richter, 2018).

This work documents version 6 of the Whole Atmosphere Community Climate Model (WACCM6) in the Community Earth System Model version 2 (CESM2). Section 2 describes WACCM6 and its role in the fully coupled Earth System Model (ESM) CESM2. We will refer to the atmosphere model as WACCM6, and the fully coupled system with that atmosphere as CESM2-WACCM6. Section 3 describes the available model configurations, and section 4 the specific simulations used in this study. Section 5 presents WACCM6 simulations, Section 6 describes differences between WACCM and the Community Atmosphere Model (CAM) versions and section 7 presents conclusions.

2. Model Description

This section documents the important features and changes to WACCM since WACCM4 (Marsh et al., 2013).

2.1. Physical Atmosphere

WACCM6 is the whole atmosphere version of the Community Atmosphere Model version 6 (CAM6). Unlike in previous versions of CESM, WACCM6 is identical to CAM6 in the range of processes that are parameterized. The only exception is the representation of parameterized gravity waves (see section 2.2). A summary of the current parameterizations for CAM6 and WACCM6 clouds and aerosols is contained in Table 1. These are detailed further below as applied to WACCM6.

Table 1 describes the different versions of WACCM starting with WACCM4, described by Marsh et al. (2013). WACCM-CCMI was developed for the Chemistry Climate Modeling Iniative (CCMI) and features updated tropospheric and stratospheric chemistry. WACCM5 (Mills et al., 2017) is based on WACCM4 chemistry, but with updated physical parameterizations following Neale et al. (2010) and features adjustments to the physical parameterizations and gravity wave schemes (section 2.2), as well as updated stratospheric prognostic aerosols (Mills et al., 2016). WACCM5 also transitions to higher horizontal and vertical resolution. WACCM-CCMI emphasized the evolution of chemistry and WACCM5 the evolution of dynamics. WACCM6 combines the new aspects of both models with additional updates for CESM2.

WACCM6 was also designed to better match CAM6 in CESM2 and uses all the same physical parameterizations as CAM6 (plus some additional gravity waves detailed in section 2.2). WACCM6 also moved to higher horizontal resolution. One of the major reasons to move to a 1° horizontal resolution for WACCM is to match the resolution of the low top model CAM6: this removes one of the major differences between CAM and WACCM. A lower resolution (2°) version of WACCM6 was released in CESM2.1.1.

2.2. Gravity Wave Drag

In addition to the orographic gravity wave drag parameterization that is identical between CAM6 and WACCM6, WACCM6 includes a nonorographic gravity wave drag parameterization following Richter et al. (2010) with separate specification of frontal and convective gravity wave sources. Two main adjustable parameters in the frontal gravity wave source specification have been changed since WACCM4 due to the increased horizontal resolution in WACCM6: The frontogenesis threshold in WACCM6 is set to 0.108 K^2 (100 km)$^{-2}$ $\cdot$h^{-1} and the source stress of frontally generated waves is set to $\tau_b = 3 \times 10^{-3}$ Pa. These parameters are the same as those used in Mills et al. (2017) for WACCM5. In order to obtain an internally generated

Table 1
Parameterizations in Different Versions of WACCM

Common name	WACCM4	WACCM-CCMI	WACCM5	WACCM6
Horizontal resolution	$1.9° \times 2.5°$	$1.9° \times 2.5°$	$0.95° \times 1.25°$	$0.95° \times 1.25°$
Vertical levels	66	66	70	70
Deep convection	ZM	ZM	ZM*	ZM*
Boundary layer	HB	HB	UW	CLUBB
Shallow convection	Hack	Hack	UW	CLUBB
Macrophysics	RK	RK	Park	CLUBB
Microphysics	RK	RK	MG2	MG2
Radiation	CAMRT	CAMRT	RRTMG	RRTMG
Aerosols	Bulk	Bulk	MAM3	MAM4
QBO	Nudged	Nudged	Interactive	Interactive
Chemical mechanism	MA(59)	TSMLT (180)	MA(59)	TSMLT1 (228)
Chemical rates	JPL-06	JPL-11	JPL-06	JPL-15
SOA	2-product	2-product	SOAG	VBS
Sulfate SAD	CCMVal2	CCMI	Interactive	Interactive
Ice SAD	Bulk	Bulk	Bulk	MG2
Solar variability	CMIP5-Solar	CCMVal2-Solar	CMIP5-Solar	CMIP6-Solar
GHG abundances	CMIP5 RCPs	CMIP5 RCPs	CMIP5 RCPs	CMIP6 SSPs
Halogens	CMIP5 RCPs	WMO 2010	CMIP5 RCPs	CMIP6 SSPs

Note. References are listed in alphabetical order: CAMRT: Collins et al. (2002), CLUBB: Bogenschutz et al. (2013), Larson et al. (2002), CMIP5 RCPs: Meinshausen et al. (2011), CMIP6: SSPs Meinshausen et al. (2017), Hack: Hack (1994), HB: Boville et al. (2006), JPL-06, JPL-11, JPL-15: Burkholder et al. (2015), MAM3: Liu et al. (2012), Mills et al. (2016), MAM4: Liu et al. (2016), Mills et al. (2016), MG2: Gettelman and Morrison (2015), Park: Park et al. (2014), RRTMG: Iacono et al. (2008), Mlawer et al. (1997), SOAG: Liu et al. (2012), UW: Park and Bretherton (2009), VBS: Hodzic et al. (2016), WMO 2010 : World Meteorological Organization (2011), ZM: Zhang and McFarlane (1995), ZM*: Zhang and McFarlane (1995), Neale et al. (2008), 2-product: Heald et al. (2008).

QBO with a reasonable period, a scaling factor of 0.25 was applied to the depth of heating in the deep convective parameterization (which reduces the effective phase speeds of convectively generated gravity waves), and the efficiency of convectively generated waves was changed to 0.4 (Mills et al., 2017).

Updated orographic schemes were implemented in WACCM6 for planetary boundary layer (PBL) form drag and orographic gravity waves (OGW). The updated PBL form drag scheme is that of Beljaars et al. (2004). The updated OGW scheme incorporates near-surface nonlinear drag processes following Scinocca and McFarlane (2000) and uses a feature-based algorithm to derive forcing data based on Bacmeister et al. (1994).

2.3. Solar and Geomagnetic Forcing

For almost all model configurations, WACCM6 uses the recommended CMIP6 solar and geomagnetic forcing as described in Matthes et al. (2017) and available via http://solarisheppa.geomar.de/cmip6. The solar spectral irradiance used to calculate heating and photolysis rates are averages from two semiempirical models: version 2 of the Naval Research Laboratory model (NRLSSI2, Coddington et al., 2015) and a composite of two Spectral And Total Irradiance REconstruction (SATIRE) models (Yeo et al., 2015). For photoionization and heating rates at wavelengths shorter than Lyman-α, WACCM6 uses the parameterization of Solomon and Qian (2005), that takes as input the $F_{10.7}$ index. Geomagnetic variability affects the flux of energetic particles that precipitate into the atmosphere, ionizing and possibly dissociating major species. Ion-pair production rates (IPR) by galactic cosmic rays, solar protons, and medium-energy electrons are also prescribed following Matthes et al. (2017). IPRs are specified on pressure levels and a magnetic latitude grid, which are interpolated to the WACCM6 geographic grid. For all chemical mechanisms other than the MAD mechanism described below, IPR rates are converted into rates of production for odd-hydrogen and odd-nitrogen species following Jackman et al. (2009).

For lower-energy electrons that precipitate in the auroral regions, WACCM6 continues to use the parameterized auroral oval model of Roble and Ridley (1994), the implementation of which in WACCM is described in Marsh et al. (2007). This model takes as input the power input to the atmosphere from energetic particle bombardment integrated over either the Northern or Southern Hemisphere, known as hemispheric power (*HP*) in gigawatts (GW). In WACCM, *HP* is assumed to be related only to the *Kp* geomagnetic index through the following revised relationship based on the formulation of Zhang and Paxton (https://doi.org/10.1016/j.jastp.2008.03.008):

$$HP(GW) = 16.82e^{0.32Kp} - 4.86 \qquad Kp \leq 7$$
$$= 153.13 + 73.4(Kp - 7.0) \quad Kp > 7$$

In the preindustrial control simulations, the solar and geomagnetic forcing are an average over the period 1850 to 1873. For transient simulations, solar and geomagnetic forcing are linearly interpolated at each model time step from daily averaged data. The model is capable of using higher-frequency forcing files, should the scientific application demand it (e.g., the modeling of solar storms).

It should be noted that beginning 1 January 2015, solar forcing data are projections based on historical solar cycles rather than from observations. It is for this reason that in non-CMIP6 simulations that are nudged to reanalysis (see section 3), WACCM6 uses only irradiance fluxes from NRLSSI2, which are updated routinely and available from National Centers for Environmental Information (data set https://doi.org/10.7289/V51J97P6).

2.4. Chemistry

WACCM6 is designed to represent a full suite of chemical constituents. It shares the four mode Modal Aerosol Model (MAM4, Liu et al., 2016; Mills et al., 2016) with CAM6 but adds chemistry (explicitly calculating the oxidants which are specified in CAM6). The baseline chemical mechanism (the collection of reactions and species) contains reactions relevant for the whole atmosphere: troposphere, stratosphere, mesosphere and lower thermosphere (TSMLT). Three additional chemistry mechanisms are available: a tropopshere and stratosphere (TS) mechanism, a middle atmosphere (MA) mechanism with a reduced set of tropospheric reactions, and the same MA mechanism with the addition of *D* region ion chemistry (MAD).

Here we describe the TSMLT mechanism used in WACCM. This is a superset of all the other mechanisms, except that it does not contain detailed *D* region ion chemistry (see below). The chemical species within this mechanism include the extended O_x, NO_x, HO_x, ClO_x, and BrO_x chemical families, along with CH_4 and its degradation products. In addition to CH_4, we also include N_2O (major source of NO_x), H_2O (major source of HO_x), plus various natural and anthropogenic precursors of the ClO_x and BrO_x families. This mechanism also includes primary nonmethane hydrocarbons and related oxygenated organic compounds. The chemical processes have evolved from previous versions (e.g., Emmons et al., 2010; Kinnison et al., 2007; Lamarque et al., 2012; Marsh et al., 2013; Tilmes et al., 2016). Reaction rates are updated following JPL 2015 recommendations (Burkholder et al., 2015).

The current mechanism includes a new detailed representation of secondary organic aerosols (SOAs) based on the volatility basis set (VBS) approach from major anthropogenic and biogenic volatile organic compound precursors (Hodzic et al., 2016). The WACCM mechanism includes a total of 231 solution species, 583 chemical reactions broken down into 150 photolysis reactions, 403 gas-phase reactions, 13 tropospheric, and 17 stratospheric heterogeneous reactions. The photolytic calculations are based on both inline chemical modules and a lookup table approach (Kinnison et al., 2007). The chemical mechanism includes two very short-lived halogens: $CHBr_3$ and CH_2Br_2. The surface mole fraction for these two species is set to 1.2 pptv (i.e., 6 pptv of total bromine). This approach adds an additional ~5 pptv of inorganic bromine to the stratosphere.

The heterogeneous reactions use aerosol surface area density (SAD) derived from MAM4 (Mills et al., 2016). The tropospheric heterogeneous reactions take four aerosol types into account (i.e., sulfate, black carbon, particulate organic matter, and secondary organic aerosol). The stratosphere heterogeneous reactions occur on three aerosol types (i.e., sulfate, nitric acid trihydrate, and water-ice). The liquid binary sulfate aerosol SAD is derived from MAM4, but modified in very cold regions (<200 K) using the Aerosol Physical Chemistry Model (Tabazadeh et al., 1994) to represent supercooled ternary solution aerosols. WACCM6 uses CMIP6 specified mixing ratios for greenhouse gases (Meinshausen et al., 2017), reactive gases and aerosols

from anthropogenic sources, including aircraft NO_x (Hoesly et al., 2018) and biomass burning (vanMarle et al., 2017). Biogenic emissions are calculated online in CLM with MEGANv2.1 (Guenther et al., 2012). Lightning NO_x emissions are interactive, and total ~3–4 TgN/year.

The water-ICE and nitric acid trihydrate SAD approach is described in Kinnison et al. (2007) with updates listed in Solomon et al. (2015). The chemical mechanism includes nine chemical tracers (SF6, O3S, E90, AOA_NH, AOA1, AOA2, ST80_25, NH5, and NH50). These tracers are described in Tilmes et al. (2016). The mesosphere and lower thermosphere chemistry component of WACCM6 includes the species and reactions described in Marsh et al. (2007). The radiatively active gases in WACCM include H_2O, O_2, CO_2, O_3, N_2O, CH_4, CFC12, aerosols, and an "equivalent CFC11" (CFC11eq), which includes radiative effects of CFC11 along with a scaling to reflect other CFCs and HFCs (Meinshausen et al., 2017).

The gas phase chemistry of the MA chemical mechanism is closer to the chemical mechanism used in WACCM4 than the TSMLT or MAD mechanisms. The MA mechamism includes two additional species not present in WACCM4. These species are the metastable states $O^+(^2D)$ and $O^+(^2P)$, which are important for the energetics of the thermosphere but do not have any impact on composition or chemistry in the lower atmosphere. As with all mechanisms, the rate coefficients have been updated to JPL-2015.

The middle atmosphere D region (MAD) chemical mechanism, which adds negative ion and cluster ion chemistry, was first implemented in WACCM4 and is described in Verronen et al. (2016). Since version 3 of WACCM, the chemical mechanism has solved for the densities of five ions and electrons that make up the E region ionosphere (Marsh et al., 2007). The MAD mechanism adds 15 positive and 21 negative ions and addresses several deficiencies in the mesosphere that occur when only E region ions are considered. The first is that the dominant negative charge carriers are no longer electrons below 75 km, but negative ions such as Cl^-(HCl), HCO_3^- and NO_3^-(HNO_3). The negative charge is balanced not by O_2^+ and NO^+, as in the E region, but by proton hydrates ($H^+(H_2O)_{n=3,4,5}$). This should yield a better representation of electron density throughout the mesosphere according to established theory (Brasseur & Solomon, 1986), though WACCM6 electron density profiles have not yet been validated against observations in the lower mesosphere. The second improvement is that production of odd-hydrogen (H, OH) and odd-nitrogen (N, NO) from ionization by energetic particles is no longer parameterized but flows through the complex chemistry following the ionization of the major species (N_2, O_2). It includes the chemistry that produces the enhanced levels of HNO_3 observed in the polar middle stratosphere following a solar storm that is not seen in simulations with the MA mechanism (e.g., Orsolini et al., 2018). Andersson et al. (2016) showed improved representation of MA chemistry with the D region ions during a solar proton event.

2.5. Prognostic Stratospheric Aerosols

WACCM6 features prognostic stratospheric aerosols. As described by Mills et al. (2016), the modal aerosol model, MAM (Liu et al., 2012, 2016) has been modified to change the mode widths and allow growth of sulfate aerosol into the coarse, or large size, mode (MAM4). This is important to properly represent aerosol sources in the stratosphere, including volcanic emissions, and natural background emissions of carbonyl sulfide (OCS), which form the stratospheric aerosol layer. Historical variability in OCS is included as a time-varying lower boundary condition (Montzka et al., 2004). SO_2 emissions from volcanic eruptions are derived from version 3.11 of Volcanic Emissions for Earth System Models Neely and Schmidt (2016, VolcanEESM). Because VolcanEESM is based on observations of volcanic SO_2 clouds weeks to months after an eruption, we must account for aerosol self-lofting due to in situ absorption of longwave radiation in estimating the initial altitude of large volcanic SO_2 clouds. For eruptions inputting more than 3.5 Tg of SO_2, we therefore impose a maximum altitude of 20 km, as discussed in Mills et al. (2016) for the case of the 1991 Pinatubo eruption. This adjustment affects four eruptions in the historical period of simulation (1850-2014): Krakatau (1883), Agung (1963), El Chichón (1982), and Pinatubo (1991).

To account for the loss of sulfur on ice and ash as observed in the initial 10 days following the 1991 Pinatubo eruption, we scale the mass input to the model by a factor of 5/9 from eruptions estimated to have emitted more than 15 Tg of SO_2. This adjustment affects two eruptions: Krakatau (1883), and Pinatubo (1991). The rationale for these altitude and mass adjustments is discussed further in Mills et al. (2016). For each day of eruption, SO_2 emissions occurs over 6 hr from 1200 to 1800 UT. A complete table of volcanic eruptions and emissions parameters is included as metadata in the VolcanEESM netCDF file used for historical simulations, which is publicly available from the CESM2 inputdata repository.

Table 2
WACCM/CAM Configurations Used in This Paper, Including cost (CPU-Hours) of the Model

	WACCM6	WACCM6-SD	CESM2-WACCM6	CESM2-WACCM6	WACCM6-SC
Name	Historical	Specified	Coupled	Coupled	Specified
Description	(AMIP)	Dynamics	1850 Control	Historical	Chemistry
WACCM component set	FWHIST	FWSD	BW1850	BWHIST	FWscHIST
CAM component set	FHIST	FWSD	B1850	BHIST	FHIST
WACCM ensembles	3	1	1	3	1
# years or dates	1950–2014	2005–2017	500 years	1850–2014	1979–2014
Coupled ocean/ice	No	No	Yes	Yes	No
Specified dynamics	No	Yes	No	No	No
Chemistry	TSMLT1	TSMLT1	TSMLT1	TSMLT1	Specified
CPU-hrs/sim-year	22,000	21,000	27,000	30,000	5,700

Following CMIP6 guidance (Eyring et al., 2016), we include in preindustrial control simulations background volcanic aerosol at a level to match average radiative forcing over the historical simulation (i.e., 1850–2014 mean). Our preindustrial control simulations therefore include constant SO_2 emission rates time-averaged from all eruptions over the historical period. SO_2 emissions from volcanic eruptions are zeroed below the tropopause in preindustrial simulations.

2.6. Secondary Organic Aerosols

WACCM6 also includes an interactive Secondary Organic Aerosol (SOA) approach based on the VBS (Tilmes et al., to be submitted) with the TSMLT mechanism. Gas phase semivolatile SOA components (SOAG) are formed from anthropogenic and biomass burning precursor emissions at the surface, as well as from biogenic emissions from the Model of Emissions of Gases and Aerosols from Nature version 2.1 (Guenther et al., 2012). In addition to the traditional SOA precursors such as isoprene, monoterpenes, aromatics, and short-chain volatile organic compounds, the updated mechanism also includes the long-chain n-alkanes (C > 12) that are not included in the standard emission inventories and that were added as coemitted species with primary organic carbon emissions from fossil fuel and biomass burning sources. This approach is more interactive than earlier approaches since the formation of organic SOA interacts with changes in the land model and climate variables. In addition, the new SOA approach includes a more comprehensive description of processes including the water solubility of intermediate organic vapors that determines their dry and wet deposition, formation of SOA by the uptake of glyoxal SOAGs into aqueous aerosols (Knote et al., 2014), and photolytic removal of particulate SOA Hodzic et al. (2015). In addition to the basic SOA scheme in WACCM6, the model can be run with an extended SOA scheme, where source contribution of different precursor emissions from biomass burning, fossil fuel, and biogenic emissions to SOA can be identified.

3. Configurations

The basic configuration of WACCM6 features ~1° (0.9° latitude × 1.25° longitude) horizontal resolution using the finite volume dynamical core (Lin & Rood, 1997). WACCM6 has 70 levels in the vertical from the surface to 6×10^{-6} hPa (~140 km). By contrast, CAM6 has 32 levels with a top at 3.6 hPa. Notably, CAM6 and WACCM6 share the same vertical level structure up to the 87 hPa level.

WACCM6 has several different baseline configurations as illustrated in Table 2. WACCM6 features one of the chemistry packages (TSMLT, TS, MA, and MAD) described in section 2.4. The baseline is TSMLT: full chemistry from the troposphere through the lower thermosphere. WACCM6 configurations with specified historical sea surface temperatures (SSTs) and ice area simulations are often termed Atmospheric Model Intercomparison Project (AMIP) simulations (component set FWHIST). WACCM6 can also be run fully coupled to active ocean and sea ice model components (Marsh et al., 2013). Coupled simulations can be configured for specific years with annually repeating boundary conditions, such as the coupled year 1850 preindustrial configuration (component set BW1850), or using time-dependent boundary conditions for greenhouse gas concentrations, aerosols, volcanic eruptions, and solar variability (component set BWHIST). Coupled simulations are termed CESM2-WACCM6. WACCM6 always runs with an interactive land surface
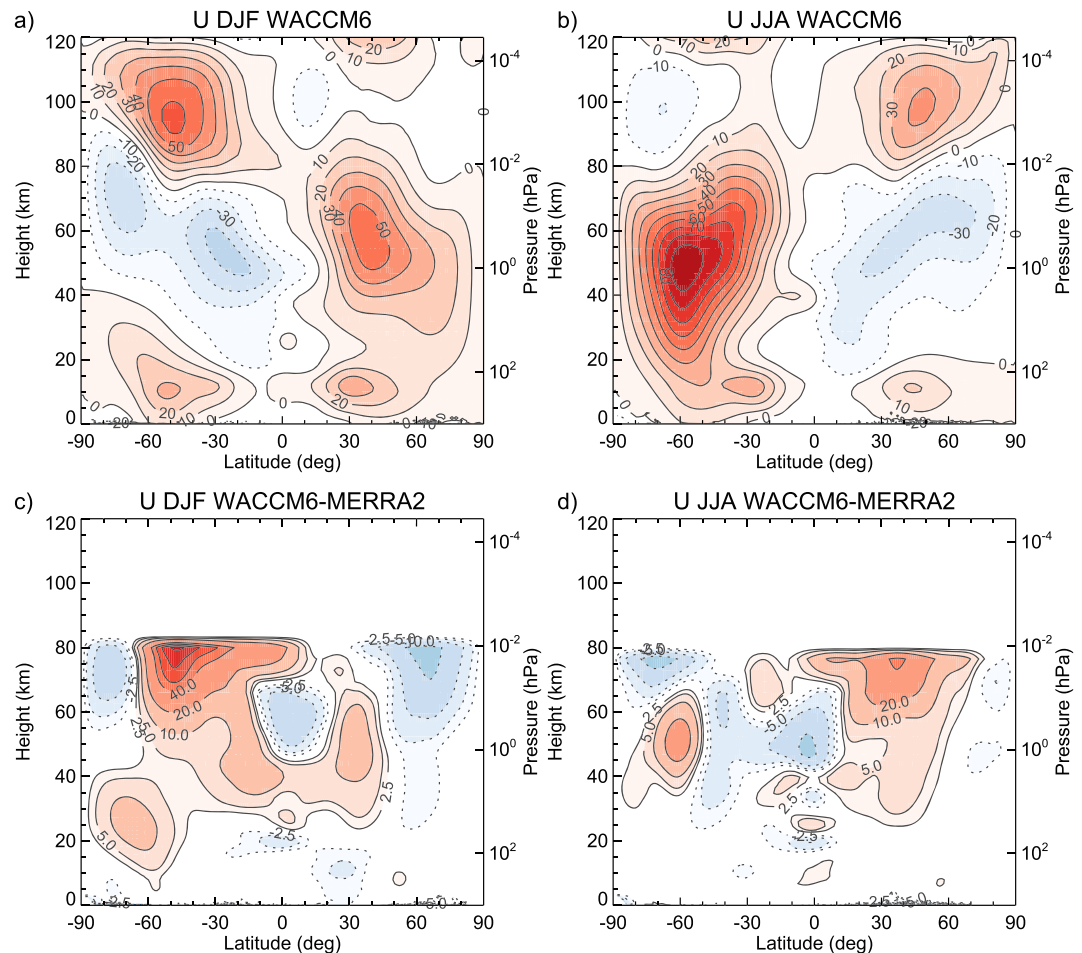
Figure 1. WACCM6 (Atmospheric Model Intercomparison Project) simulation zonal wind for (a) December, January, February (DJF) and (b) June, July, August (JJA). Contour interval of 10 m/s. Differences between WACCM and MERRA2 Reanalysis for (c) DJF and (d) JJA. Variable contour interval of ±2.5,5,10,20,40 m/s.

model (the Community Land Model version 5, or CLM5). The coupled preindustrial control (BW1850), coupled historical (BWHIST), and historical fixed SST or AMIP simulations (FWHIST) are simulations in support of the CMIP6 core ("DECK") experiments.

WACCM6 can also be run in a nudged, or specified dynamics (SD) configuration (WACCM6-SD). For WACCM6-SD simulations (component set FWSD), winds and temperatures are relaxed to a specified set of data, typically another model or a reanalysis system. Commonly, the NASA Goddard Earth Observation System (GEOS) model analyses, Modern-Era Retrospective analysis for Research and Applications (MERRA) (Rienecker et al., 2011) or MERRA2 Molod et al. (2015) are used. This SD version is effective for reducing climate noise, reducing biases in winds and/or temperatures, and reproducing the chemical response to specific events or for specific times, such as comparison to specific field programs or individual observations. WACCM6-SD configurations typically use a vertical level structure taken from the source nudging data.

As described in Smith et al. (2014), WACCM can also be run with specified chemistry (SC), or WACCM6-SC. In WACCM6-SC simulations (compset FWscHIST), radiatively active chemical species (like ozone) are prescribed, typically from a WACCM6 run with interactive chemistry, while all other CAM6 and WACCM6 parameterizations for clouds are interactive. The aerosol model is also reduced in complexity for WACCM6-SC, using CAM6 aerosols (simplified SOA and prescribed stratospheric aerosols). WACCM6-SC is an efficient model useful for dynamical studies. An example of the use of WACCM6-SC for understanding dynamical and chemical effects are provided in section 6.
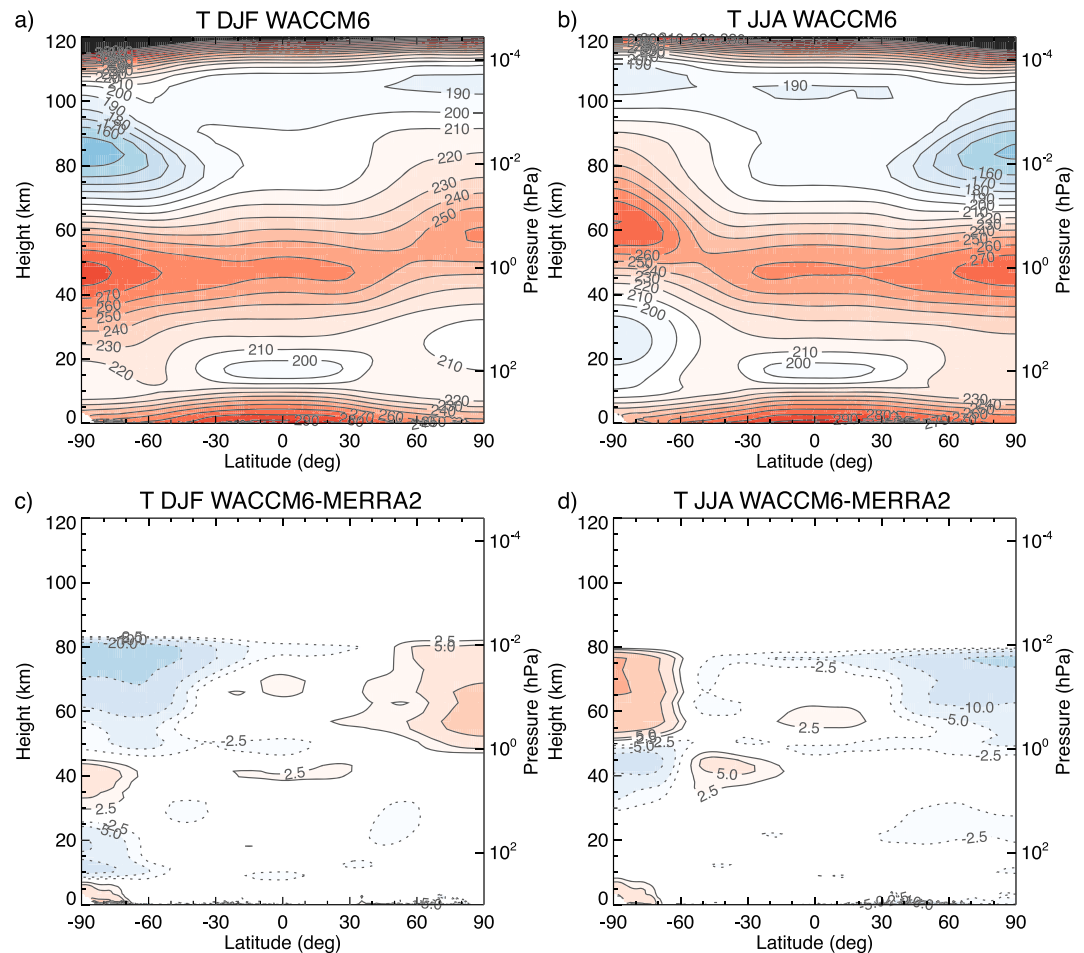
Figure 2. WACCM6 (Atmospheric Model Intercomparison Project) simulation temperatures for (a) December, January, February (DJF) and (b) June, July, August (JJA). Contour interval of 10 K. Differences between WACCM and MERRA2 Reanalysis for (c) DJF and (d) JJA. Variable contour interval of ±2.5,5,10,20 K.

For comparison, we also perform CAM6 AMIP simulations with specified SST and ice (component set FHIST). CAM6 has the same physical parameterization suite as WACCM6 minus the frontal and convective gravity wave drag schemes, with a lower top, loss of several upper atmosphere processes, fewer levels, and no chemistry. CAM6 is essentially WACCM6-SC with a lower lid (and without the convective and frontal gravity waves). Comparisons between WACCM6, WACCM6-SC, and CAM6 can illustrate the impact of chemistry-climate coupling (WACCM6 vs. WACCM6-SC), the impact of the broader vertical range (WACCM6-SC vs. CAM6) or both (WACCM6 vs. CAM6).

Table 2 also shows the model cost. Coupled simulations are more expensive, and WACCM6-SC reduces the cost by a factor of 4 due to removal of the TSMLT chemistry. WACCM-CCMI or WACCM4 costs about 2,500 CPU-hr/sim-year, due to lower resolution (2°), simpler chemistry (MA), and simpler physics (CAM4 vs. CAM6).

WACCM6 now has the option to run with a more complete thermosphere and ionosphere, with a lid near 500km. This extended version, or WACCM-X, currently is coupled to WACCM4 physics and is described in a companion paper by Liu et al. (2018).

4. Simulation Description

Results documented below (section 5) are based on the simulations with WACCM6 listed in Table 2. All are at 0.9° × 1.25° horizontal resolution and 70 vertical levels, with TSMLT chemistry, and all are coupled actively to the CLM5 land model. Fully coupled CESM2-WACCM6 is run first for a long control run
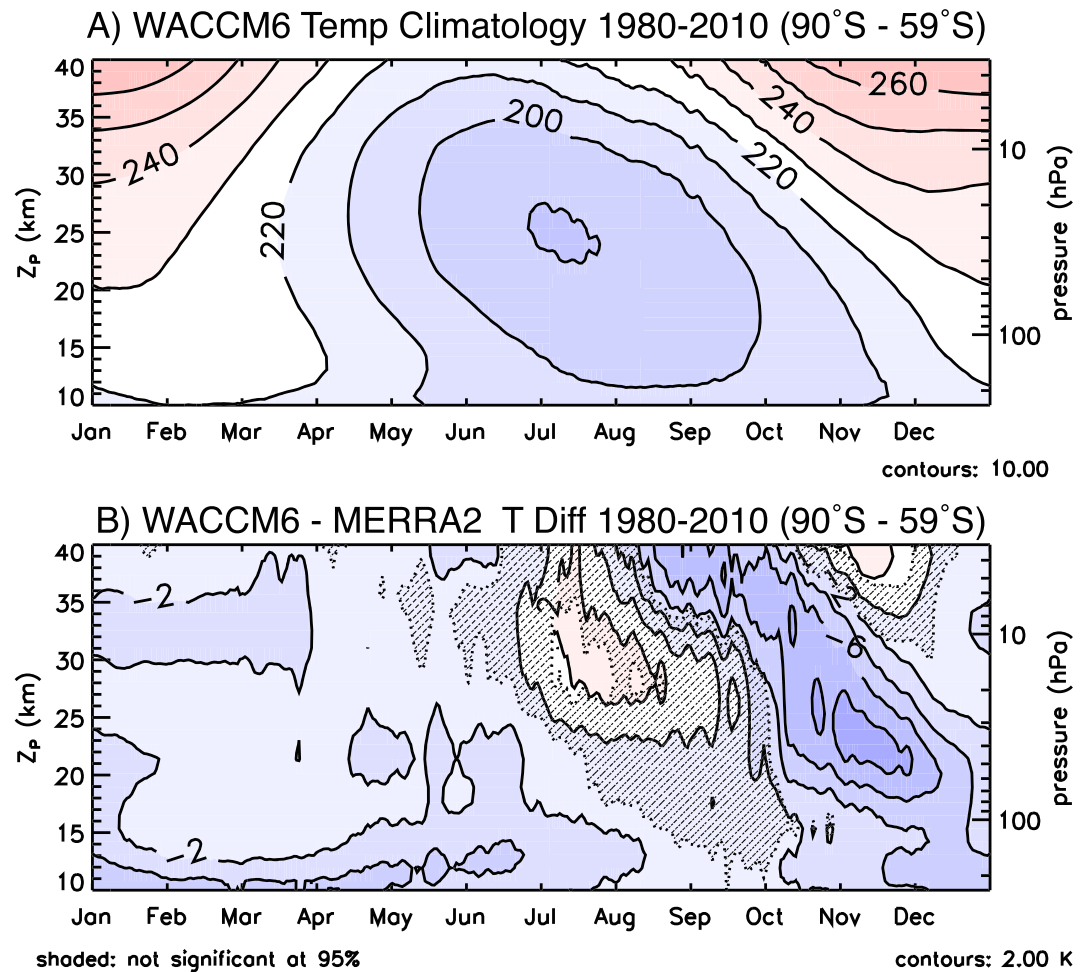
Figure 3. WACCM6 (Atmospheric Model Intercomparison Project) simulation (a) Climatological (1980–2010) Southern Hemisphere Polar Cap (90–59°S) temperature evolution. Contour interval of 10 K. (b) Difference versus MERRA2 reanalysis. Shaded differences are not significant at the 95% level based on a *t* test. Contour interval of 2 K.

representing preindustrial (1850) conditions and starting from a 200 year control simulation with CESM2-CAM6. Then three coupled simulations with transient forcing from the Coupled Model Intercomparison Project round 6 (CMIP6) (Eyring et al., 2016) from 1850–2014 are initialized from year 56, 61, and 70 of this CESM2-WACCM6 run. WACCM6 is also run with prescribed SST and sea ice distribution and CMIP6 forcing for greenhouse gases and aerosols over the period from 1950–2014, initialized with land and atmospheric initial conditions from coupled simulations. A WACCM6-SD simulation is forced with MERRA2 analysis over the more recent period when comprehensive satellite data are available (1980 to 2014) to examine chemistry with dynamic variability prescribed from the historical atmosphere (as conditioned by a reanalysis system). WACCM6-SC is run with specified SSTs and chemical fields from the WACCM6 AMIP simulations.

5. Results

Here we present key results from WACCM6, focusing on the stratosphere. The overall WACCM6 tropospheric climatology and climate are described in section 6 with a comparison to CAM6.

5.1. Climatology/Annual Cycle

WACCM6 is able to effectively simulate the zonal winds from the surface through the mesosphere. Figure 1 illustrates the December, January, February (DJF) and June, July, August (JJA) WACCM6 climatological zonal wind, and compares it to MERRA2 reanalysis (Rienecker et al., 2011). Note that MERRA2 only goes
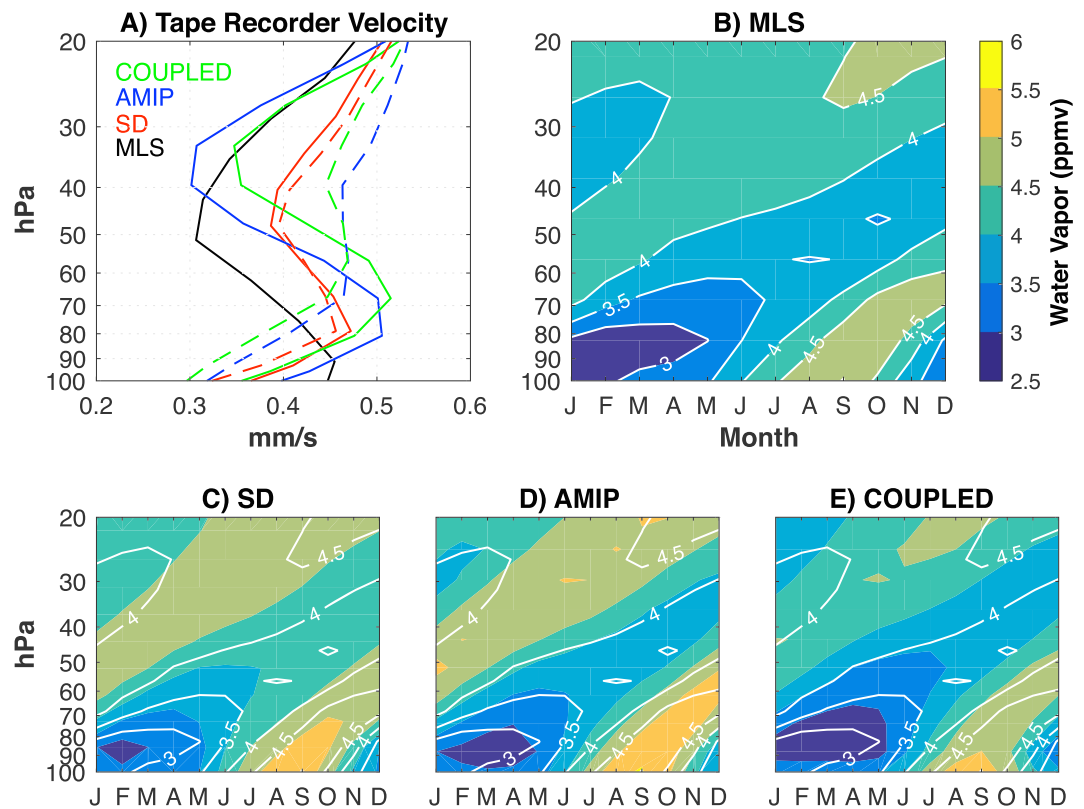
Figure 4. (a) Tape recorder velocity (mm/s) averaged over 2005–2014 from MLS satellite observations (black), specified dynamics WACCM-SD (red), specified SST WACCM6 (AMIP-blue), and coupled WACCM6 run (COUPLED-green). WACCM6 solid lines, WACCM4 dashed lines. (b) Composite MLS water vapor annual cycle showing the "tape recorder" of low and high water vapor being advected in the vertical circulation of the stratosphere. (c–e) Composite water vapor annual cycles (contour shading) with MLS annual cycle (white contours). (c) Specified dynamics WACCM6 (SD), (d) free running specified SST WACCM6 (AMIP) and (e) coupled CESM2-WACCM6 historical run (COUPLED).

up to 80 km, so there are no comparisons above that. Also note the 50–80 km region is very model dependent, and MERRA2 may not be the "truth." There are ~5 m/s biases in Southern Hemisphere winter zonal wind in the lower stratosphere, but, in general, the mean wind speeds compare well to reanalyses. Biases would be expected to become larger with altitude as the wind speed increases, and also because there are fewer observational constraints on reanalysis at high latitudes, and it is just a WACCM6 to reanalysis model (MERRA2) comparison. WACCM6 is able to simulate the seasonal variation of the stratospheric polar jets.

WACCM6 is also able to effectively simulate the temperature structure from the surface through the mesosphere. Figure 2 illustrates DJF and JJA WACCM6 climatological temperature compared to MERRA2 (Rienecker et al., 2011). Seasonal mean tropical tropopause temperatures are within ±2 K of the reanalysis. There are winter time biases in the Southern Hemisphere temperature in the lower stratosphere, consistent with the zonal wind biases (Figure 1). WACCM6 also has a cold summer mesopause at ~85km with temperatures close to 140 K, similar to observations.

The winter (JJA) seasonal temperature biases over the South Pole in Figure 2d increase and propagate downward in spring, as illustrated in Figure 3. These biases result from remnants of the winter jet in the lower stratosphere persisting too late. The biases occur late enough in the spring that they do not impact lower stratosphere southern polar springtime ozone depletion (see below). This bias reflects a delayed breakdown of the Southern Hemisphere polar vortex relative to observations (Butchart et al., 2011).

The annual cycle of tropical stratospheric water vapor is illustrated in Figure 4, with a representation of the water vapor "tape-recorder" (Mote et al., 1996). WACCM6 is compared to an observational climatology from the AURA Microwave Limb Sounder (MLS, Read et al., 2007; Waters et al., 2006), illustrated in Figure 4b. The tape recorder vertical propagation speed based on tracer contour advection is slightly faster and shifted slightly upward relative to observations (Figure 4a). The amplitude of the tape recorder is well represented,
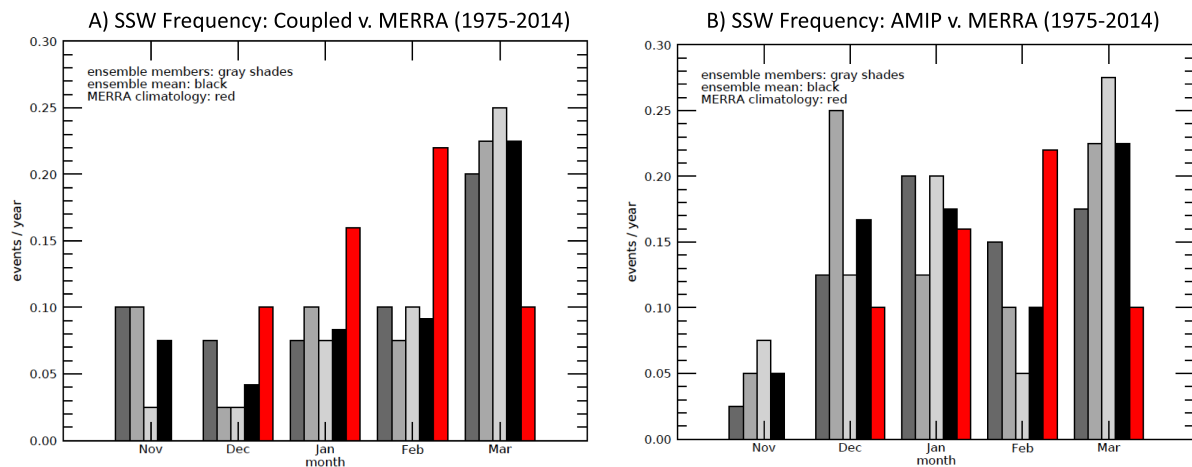
Figure 5. Northern Hemisphere winter stratospheric sudden warmings frequency by month for (a) coupled and (b) Atmospheric Model Intercomparison Project fixed sea surface temperature WACCM6 simulations (gray shading = ensembles, black = mean), and MERRA reanalyses (red).

with a 0.25–0.5 ppm high (moist) bias in WACCM6. Specified Dynamics (SD) simulations (Figure 4c) have a slightly lower velocity but higher bias than either fixed SST (AMIP, Figure 4d) or coupled (COUPLED, Figure 4e) simulations. Free running coupled simulations (Figure 4e) have small biases in value or amplitude relative to MLS. We will discuss differences between WACCM6 (solid lines in Figure 4a) and WACCM4 (dashed lines in Figure 4a) in section 6.

WACCM6 also does a good job at reproducing the distribution of ozone in the stratosphere. This will be discussed in more detail in the analysis of the evolution of stratospheric ozone over the late twentieth century in section 5.3.

5.2. Variability

One of the major features of intraseasonal variability in the stratosphere is Northern Hemisphere (NH) Stratospheric Sudden Warmings (SSWs) which can have impacts all the way down to the surface (Baldwin & Dunkerton, 2001). In this case we define an SSW by a wind reversal (McTurf, 1978), specifically a period when the 10 hPa zonal mean zonal wind at 60°N is <0 m/s (i.e., eastward) following Charlton and Polvani [2007]. Specifics of the SSW frequency might vary with metric, but we diagnose model and reanalysis in the same way, so we would not expect this to impact model biases. Figure 5 indicates that the coupled (Figure 5a) and historical fixed SST or AMIP (Figure 5b) WACCM6 ensembles are able to capture the frequency of SSWs averaged over 30 years (1980–2010). The ensemble mean frequency (black bars) is close to observations. While Ayarzagüena et al. (2019) have noted that there are differences in the timing and frequency distribution of SSWs in "observations" (different reanalyses), this does not affect the conclusions here. Results are the same with NCEP reanalyses over the satellite era. The AMIP simulations have too few SSWs in February and too many in March (Figure 5b) while coupled cases (Figure 5a) also have too few SSWs in January and February. The high March frequency may be a result of a late bias in the spring polar vortex breakup, but it is also clear from the spread among WACCM ensemble members that the observed record is likely subject to considerable sampling uncertainty. The total winter frequency is 0.58 warmings per year in MERRA, 0.60 with NCEP, with 0.72 per year for the historical SST, and 0.52 per year for the coupled model, bracketing the observations. The interannual standard deviation in SSW frequency is 0.7 per year, based on counting events each year. de la Torre et al. (2012) used a different method and found that the 5–95 percentile spread in WACCM4 SSW frequency in any month was ±0.1 per year. For WACCM4, the frequency of occurrence of SSWs was 0.46 per year with a range across ensembles of 0.33 to 0.53 per year (Marsh et al., 2013).

WACCM6 is also able to simulate, albeit imperfectly, the quasi-biennial oscillation (QBO; Figure 6), the equatorial zonal wind propagation, which in observations has an average period of ~28 months. Similar to WACCM5 (Mills et al., 2017), WACCM6 simulates a reasonable QBO with 70 levels in a free running configuration. The average QBO period calculated using Fourier analysis is 29 months for WACCM6 (fixed SST), 27 months for WACCM6 (coupled ocean) compared to 28 months for ERAI reanalysis. But the QBO amplitude is too weak in the lower stratosphere and the QBO does not extend low enough in the stratosphere
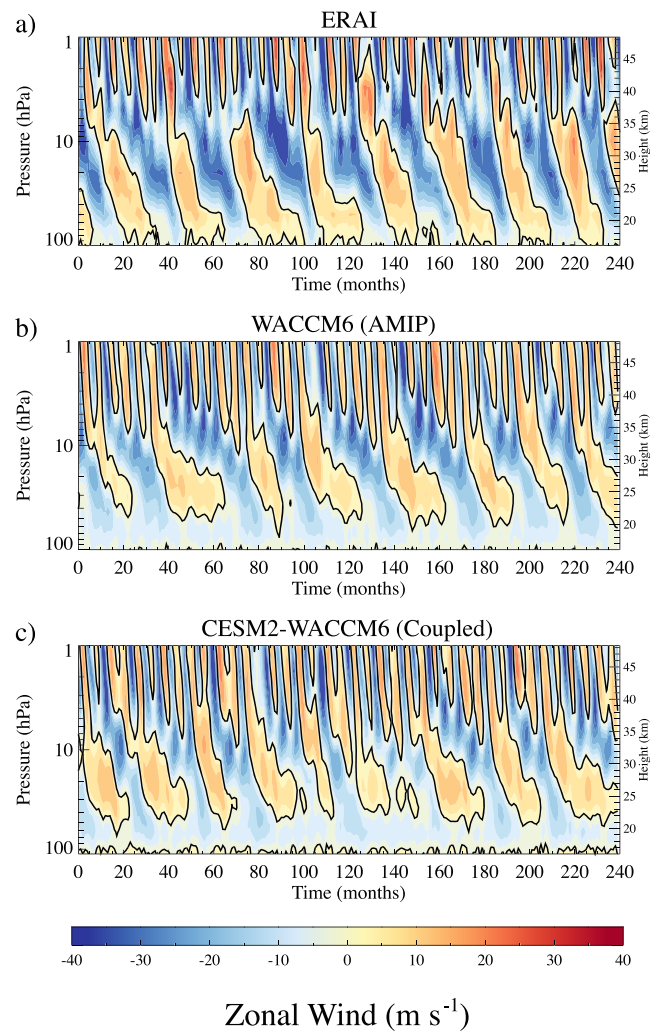
Figure 6. Monthly average zonal wind from 10°S–10°N in (a) European Center Reanalysis (ERAI), (b) WACCM6 historical simulation with historical SSTs, and (c) fully coupled WACCM6 historical simulation illustrating the quasi-biennial oscillation.

(Figures 6b and 6c) compared to observations (Figure 6a). This deficiency is due to the relatively coarse vertical resolution in the lower stratosphere in this version of the model likely impacting equatorial gravity wave momentum deposition. More realistic downward propagation of the QBO can be obtained in WACCM with increased vertical resolution (Garcia & Richter, 2018). The QBO deficiencies might impact QBO teleconnections to high latitudes, but the problem is likely that wave-mean flow interactions with parameterized equatorial gravity waves require high vertical resolution.

WACCM6 does not perform as well in reproducing the semi-annual oscillation (SAO) in stratospheric and lower mesospheric zonal wind at higher altitudes except at the stratopause, as illustrated in Figure 7, which compares model winds at the equator with winds derived from SABER satellite data (Smith et al., 2017). The timing of the SAO minimum winds at solstices in the upper stratosphere is early by less than a month and has a similar shift with pressure to that determined from stratospheric observations. The SAO near the stratopause is driven primarily by horizontal advection of zonal mean momentum that varies with seasonal changes in the Brewer-Dobson circulation. However, wind variations in the mesosphere simulated by WACCM6 are overall much weaker than those deduced from observations, and the timing of the oscillation in the mesosphere is out of phase with observations. This may be due to a deficiency in forcing by tropical waves and could also be a result of coarse vertical resolution. There is not currently an observational base to determine whether the waves driving winds in the tropical upper stratosphere and lower mesosphere are small-scale gravity waves or larger-scale waves, such as equatorially trapped Kelvin waves.
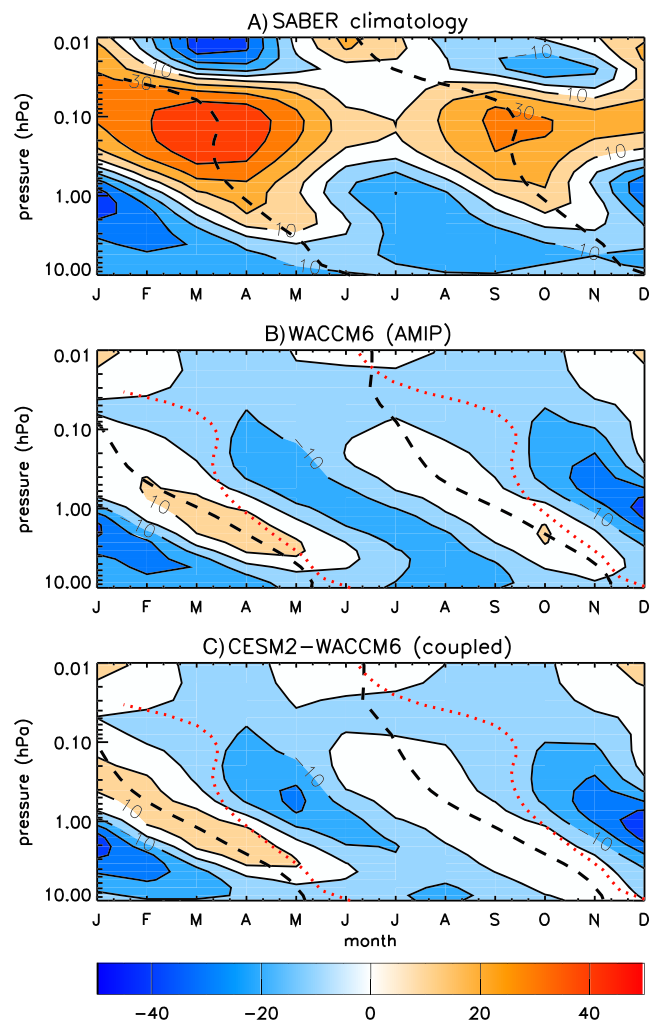
Figure 7. Monthly average zonal wind from 10°S–10°N in (a) SABER satellite observations, (b) WACCM6 (AMIP), and (c) fully coupled WACCM6 historical simulation illustrating the semi-annual oscillation (SAO). The black dashed lines show the SAO phase and the red dotted lines on (b) and (c) show the phase from (a) for comparison.

WACCM6 represents impacts of both large (e.g., Pinatubo, 1991) and many small-to-moderate (e.g., 2005–2014) eruptions. Figure 8 shows simulated and observed stratospheric aerosol optical depth (SAOD) from 1980–2015 at different locations corresponding to ground-based lidar observations using a backscatter-to-extinction ratio of 50. WACCM6 with prognostic stratospheric sulfur is able to produce the correct SAOD from volcanic eruptions over most latitudes. There are some differences in the tropics (Mauna Loa) during the volcanically quiescent period of 1997–2004, and in the Southern Hemisphere (Lauder) during the recent period of small-to-moderate eruptions.

5.3. Trends

WACCM6 is able to reproduce the evolution of the ozone layer, including the Southern Hemisphere polar ozone hole (World Meteorological Organization, 2011), as illustrated in Figure 9. The observations lie within the range of variability spanned by the coupled and fixed SST (AMIP) simulations. WACCM-SD simulations with imposed variability (purple in Figure 9) are able to reproduce the interannual variability seen in observations (black in Figure 9). Variability at both poles (Figures 9a and 9b) is reproduced, including low ozone events in the NH (Figure 9b). There are some biases in midlatitudes in free running simulations (Figures 9c and 9d), which are not seen in SD simulations. Larger biases occur in the tropics (Figure 9e).

The reason for the tropical differences is related to tropical upwelling, illustrated in Figure 10, and consistent with Figure 4. In the 20°S–20°N region, the vertical velocity is larger for pressures greater than 50 hPa for the coupled case and the AMIP case than the SD case. SD is similar to a direct calculation from MERRA2
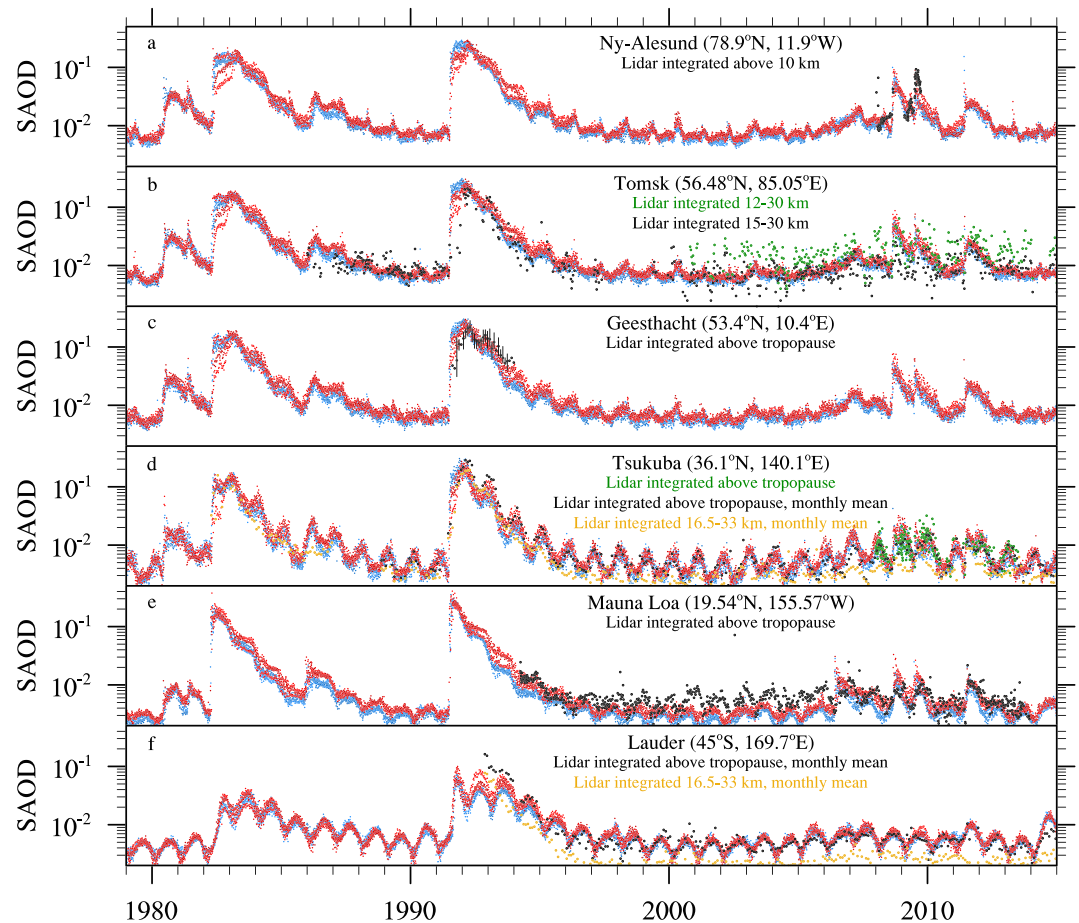
Figure 8. Five-day averaged stratospheric aerosol optical depth (SAOD; above model tropopause) from coupled (blue) and AMIP (red) ensembles compared to lidar observations (green, black, yellow). (a) Ny Alesund (78.9°N, 11.9°W) above 10 km (black, Ridley et al., 2014). (b) Tomsk (56.5°N, 85.0°E) 15–30 km 10-day averages from Jan 1986 to Dec 2014 (black, Zuev et al., 2017), and 12–30 km 10-day averages from Jan 2006 to Dec 2013 (green). (c) Geesthacht (53.4°N, 10.4°E) above the tropopause (black with 1-σ error bars, Ansmann et al., 1997). (d) Tsukuba (36.1°N, 140.1°E) 15–30 km monthly averages from Apr 1982 to Dec 2014 (yellow circles), above the tropopause monthly averages from Nov 1988 to Dec 2014 (black, Sakai et al., 2016), and above the tropopause daily from Jan 2008 to Jul 2013 (green). (e) Mauna Loa (19.5°N, 155.6°W) above the tropopause (black), Hofmann et al. (2009). (f) Lauder (45.0°S, 169.7°E) monthly averages from Nov 1992 to Dec 2014, 16.5–33 km (yellow) and above the tropopause (black) Sakai et al. (2016).

output. Since the lower stratospheric ozone field is dynamically controlled, the vertical velocity will impact the total column ozone. The larger vertical velocities in the lower stratosphere are expected to be associated with reduced ozone due to vertical advection of ozone poor air from the troposphere. The difference in vertical velocity would result in more O_3 in the SD case than free running for pressures greater than 50 hPa. The opposite is the case for pressures between 50 and 10 hPa, broadly consistent with the representation of tropical upwelling between the two cases. Tropical anomalies (Figure 9e) will affect the midlatitudes (Figures 9C and 9d) as well as the near-global (60°S–60°N) total column ozone (Figure 9f).

Globally averaged surface temperature in the CESM2-WACCM6 fully coupled simulations for the historical period (1850–2014) are compared to observations and CESM2-CAM6 simulations in Figure 11. Both CESM2-WACCM6 and CESM2-CAM6 are able to reproduce the observed historical evolution of global mean surface temperature anomalies. Notably, CESM2-WACCM6 global mean surface temperature does not have a different mean (not shown) or global variability than CESM2-CAM6 simulations. Note how in the first 80 years of this record from 1850–1930 or so, when radiative forcing was dominated by volcanic eruptions, both CESM2-CAM6 and CESM2-WACCM6 track much of the observed decadal variability, indicating that it was likely forced variability and associated with volcanoes. Also note that there is a spread of variation
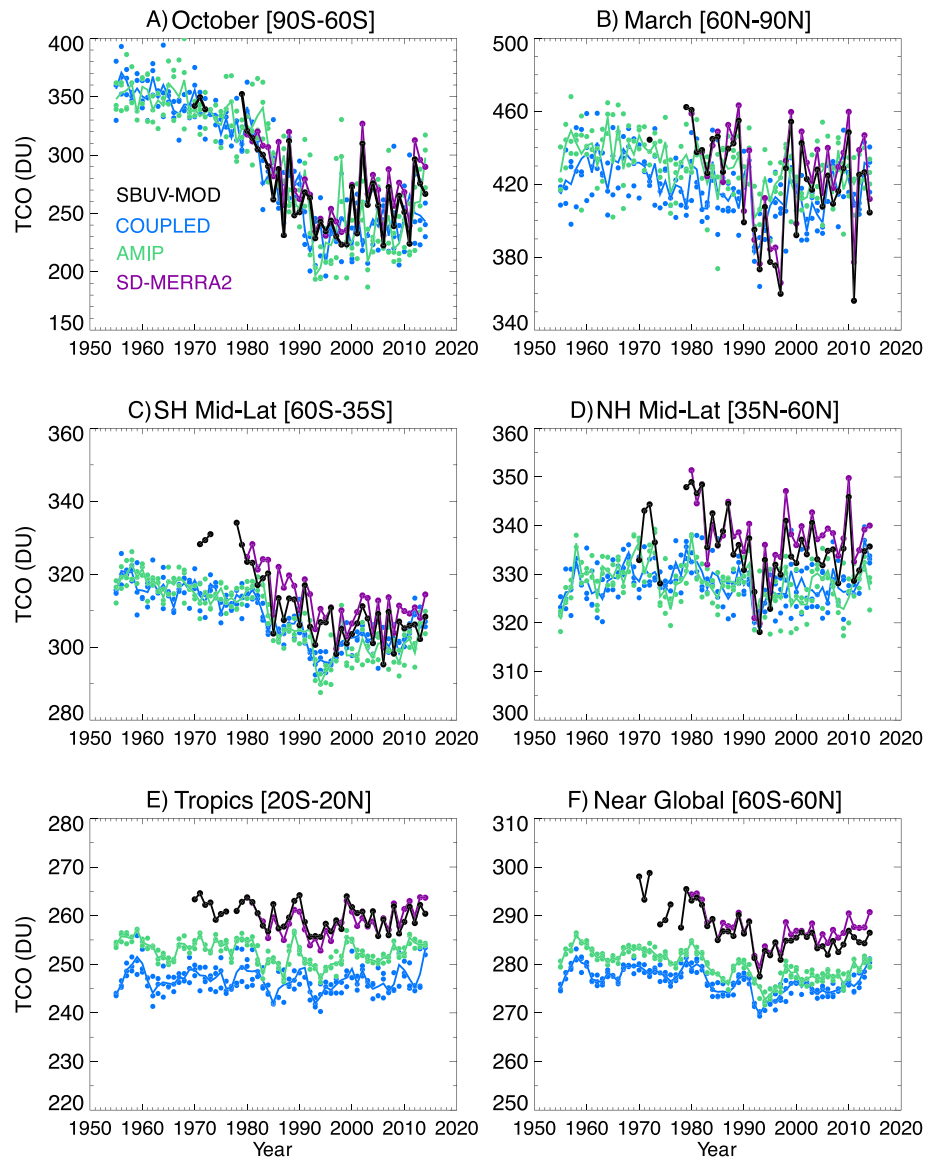
Figure 9. Total column ozone (in Dobson Units: DU) from WACCM6 coupled simulations (COUPLED: blue), specified SST (AMIP) simulations (green), specified dynamics simulation (SD-MERRA2: purple), and observations (SBUV-MOD: black). Individual points are symbols, mean across ensembles solid line. (a) October 90–60°S, (b) March 60–90°N, (c) annual 65–35°S, (d) annual 35–60°N, (e) annual 20°S–20°N, and (f) annual 60°S–60°N.

of volcanic response in CESM2-WACCM6 to large volcanoes such as Krakatoa in 1883. Volcanic SAOD is shown on the top of Figure 11. The CESM2 historical ensemble used volcanic forcing equal to the average of the three coupled CESM2-WACCM ensemble members.

Figure 12 illustrates stratospheric temperature trends from WACCM6 historical AMIP simulations compared to stratospheric sounding unit (SSU) and the advanced microwave sounding unit (MSU) temperatures (Randel et al., 2017). As with WACCM4 Randel et al. (2017, Figure 1), WACCM6 is able to capture stratospheric temperature trends from 1980–2014. WACCM6 has a slightly better representation of the temperature response to the 1991 Mount Pinatubo eruption. As noted by Randel et al. (2017), temperature trends are a combination of effects from ozone depletion and recovery and increasing greenhouse gases, which WACCM6 captures well. Variability is forced from volcanic eruptions and the tropospheric El Niño–Southern Oscillation, which is imposed on the WACCM6 AMIP simulations with observed SSTs.
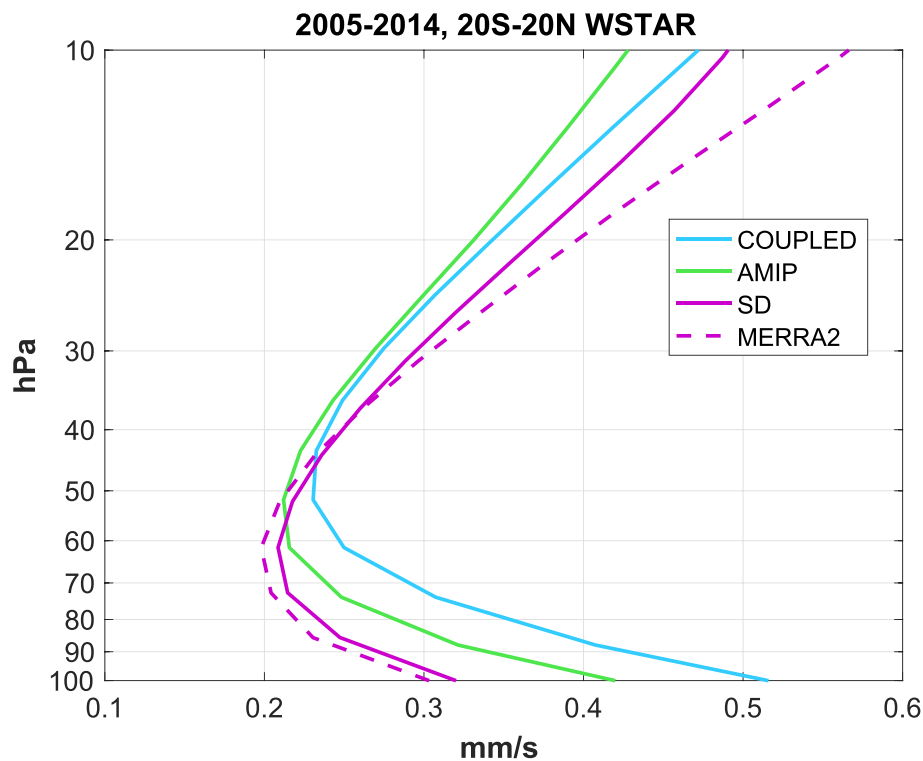
Figure 10. Tropical (20°S–20°N) averaged upwelling (W*: TEM residual vertical velocity in mm/s). WACCM6 coupled simulations (blue), specified SST AMIP simulations (green), specified dynamics simulation with MERRA2 winds and temperatures (SD, purple). The w* is calculated directly from MERRA-2 purple dash.

6. Difference Between WACCM Versions and Configurations

Figure 11 illustrates transient differences in global mean temperature anomalies between CESM2-CAM6 and CESM2-WACCM6 simulations. Table 3 illustrates differences in global mean climate metrics between different configurations for the historical period (2000–2014) as well as overlapping observations. The observational uncertainty on the radiative flux products is about ±2 W/m² , based on the bias errors from Loeb et al. (2009), Table 2. For global mean cloud fractions, the two standard deviation interannual variance is 0.3%. Here we compare both CESM2-CAM6 and CESM2-WACCM6, and the previous version of WACCM, WACCM4-CCMI. Table 3 also shows preindustrial (PI, from B1850 simulations) values from CESM2-WACCM6, CESM2-CAM6, and CESM1-WACCM4. With respect to many of the radiative fluxes, WACCM6 and CAM6 fall within the range of uncertainty. WACCM4 is significantly different for all but clear sky longwave radiation (FLNTC). WACCM6 is thus demonstrably improved in most respects for cloud and radiative budgets.

6.1. WACCM6 Versus CAM6

WACCM6 and CAM6 have very similar climates defined by their top of atmosphere energy budget and cloud radiative effects. WACCM6 of course provides significantly more fidelity in the stratosphere as it represents the meridional overturning circulation of the stratosphere fully, as well as full tropospheric and stratospheric chemistry, with interactive oxidants and ozone. Differences between WACCM6 and CAM6 are thus a combination of differences due to the different lid and upper atmospheric processes with the differences in chemistry and aerosols. The tropospheric physical processes are the same between WACCM6 and CAM6. We discuss these differences below and also refer to a WACCM-SC (Specified Chemistry) simulation where appropriate to help distinguish dynamical from chemical and aerosol processes.

There are several climate differences between CAM6 and WACCM6. In the clear sky, there is a −2 W/m² top of model difference in both the SW net flux (FSNTC) and LW net flux (FLNTC) in WACCM6 versus CAM6. This is likely due to absorption of radiation occurring above the model top of CAM, despite an effort to parameterize this absorption in CAM.
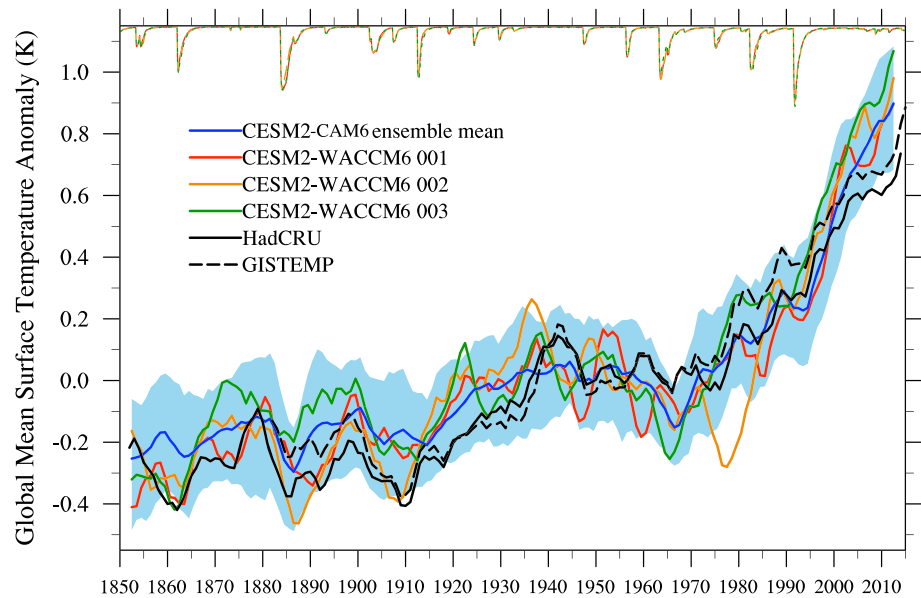
Figure 11. Global mean surface temperature anomalies with respect to the 1920–1980 average with 5 year smoothing. Blue: mean of 10-member CESM2 historical ensemble (blue shading shows the ensemble spread). Three coupled CESM2-WACCM historical ensemble members are red (001), orange (002), and green (003) curves. Observed temperatures from Hadley Centre-Climatic Research Unit Version 4 (HadCRUT4) infilled with kriging (Cowtan & Way, 2014) (black solid). Goddard Institute for Space Studies (GISS) Surface Temperature Analysis (Hansen et al., 2010) (black dashed). Top curves are a stratospheric aerosol optical depth index (1.15–2 × global average) for each coupled CESM2-WACCM ensemble member.

Table 3 also indicates a 1 W/m^2 magnitude increase in SW (negative) and LW (positive) cloud forcing (SWCRE and LWCRE) in WACCM. This comes from high clouds in the tropics, where there is an increase in high cloudiness (CLDHGH) at the edges of the tropics, and an increase in ice water path (IWP) and overall ice crystal number. This would appear to be a result of an increase in accumulation mode sulfate in the tropics causing increased homogeneous nucleation of cirrus ice crystals. The increased sulfate is from (a) DMS (dimethylsulfide) sources and (b) stratospheric volcanic sulfate in WACCM6 which are not present in CAM6. CAM6 takes in prescribed surface area densities of sulfate from WACCM6, but not the actual sulfate which can impact tropospheric clouds.

There are also small increases in high-latitude NH shortwave cloud forcing (SWCRE) in WACCM6 over CAM6, due to increases in cloud droplet number from increased East Asian aerosol burdens which extend into the Arctic. Aerosol lifetimes also differ in the tropics in WACCM6 due to differences in tropospheric chemistry and removal of oxygenated organics.

CESM2-CAM6 and CESM2-WACCM6 have similar preindustrial (1850) annual mean sea ice extent (SIE), but the SIE is much less than WACCM4 (Table 3). The main difference in SIE between CESM2-CAM6 and CESM2-WACCM6 is in summer when the CESM2-WACCM6 simulations have much less melt, but the annual mean SIE is not very different. As a result, there are larger differences between CESM2-CAM6 and CESM2-WACCM6 in preindustrial sea ice volume (SIV) in Table 3. Less melt means sea ice remains around for the subsequent winter and thus the ice is thicker.

In coupled CESM2-WACCM6 simulations, the recent twentieth century warming makes these differences more apparent (Figure 13). CESM2-WACCM6 has higher September NH SIE than CESM2-CAM6, in better agreement with observations (Figure 13a). CESM2-WACCM6 and CESM2-CAM6 NH SIE are close in March (the month of maximum sea ice, Figure 13a). CESM2-WACCM6 annual NH sea ice volume (Figure 13b) is dropping slightly faster than observations, while CESM2-CAM6 has lower ice volume, but a decline rate is similar to observed. CESM2-WACCM6 is a bit colder than CAM in the 1960–1980 period, and warming up faster. Analysis (not shown) indicates that in 2000–2014, there is less downward surface SW and LW in CESM2-WACCM6, and that this happens because of slightly higher LWP (in winter around the ice edge, in summer over the ice). Higher LWP in CESM2-WACCM6 than CESM2-CAM6 results from higher aerosol
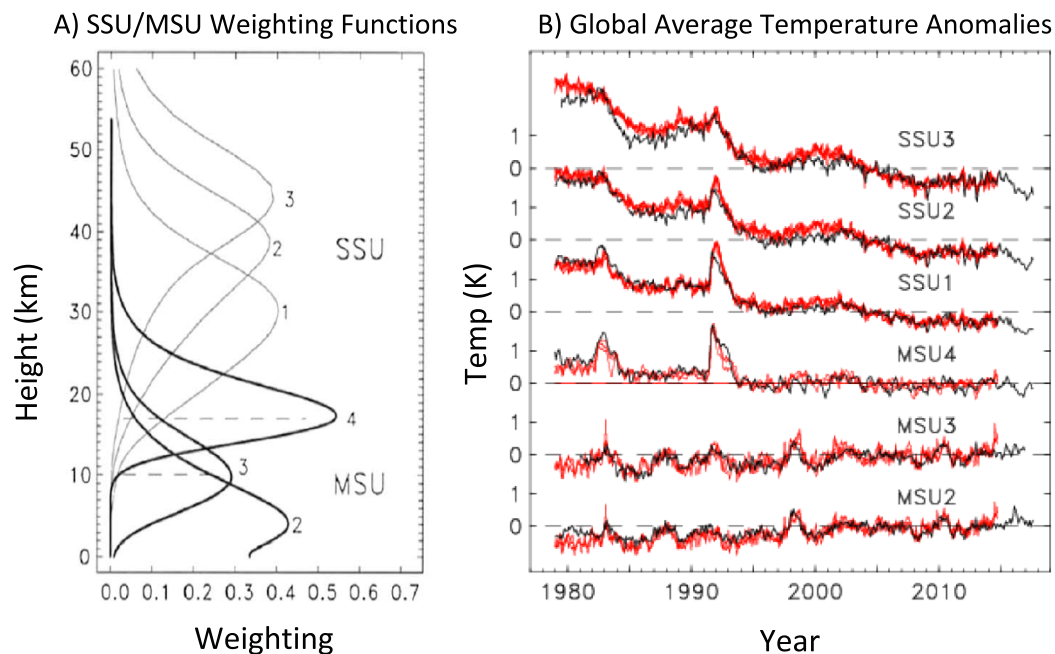
Figure 12. (a) MSU and SSU weighting functions from Randel et al. (2017). (b) Global average temperature time series from three WACCM6 specified SST (AMIP) ensembles convolved with SSU or MSU weigthing functions (red). SSU or MSU observations (black).

number. The higher aerosol number increases cloud condensation nuclei and cloud drop number, resulting in smaller drops that do not precipitate as readily. Thus, the tropospheric aerosol chemistry impacts Arctic sea ice.

CESM2-WACCM6 and CESM2-CAM6 climate variability metrics are also very similar, with very few statistical differences. CESM2-WACCM6 however does have better high-latitude surface pressure variability, as illustrated in Figure 14. Other ensemble members are similar. CESM2-WACCM6 has improved NH high-latitude surface variability by this metric compared to CESM2-CAM6, despite the same vertical resolution in the troposphere. Area-weighted pattern correlations and root-mean-square differences for the standard deviation of sea level pressure were calculated between observations (ERA Interim and twentieth century reanalyses) and three ensemble members for CESM2-WACCM6 and CESM2-CAM6 coupled experiments. December–February pattern correlations are as high for CESM2-WACCM6 (0.96) as for other reanalyses (0.95–0.96) and higher than for CESM2-CAM6 (0.93–0.95). Root-mean-square differences are 0.10–0.12 for other reanalyses relative to ERA, 0.11–0.12 for CESM2-WACCM6, and 0.12–0.14 for CESM2-CAM6 ensemble members. This variability improvement is present across three CESM2-WACCM6 twentieth century ensemble members compared to nine CESM2-CAM6 ensemble members. The difference is likely related to slight changes in the Northern Annular Mode (NAM) pattern in the stratosphere and indicates the importance of resolving stratospheric variability. WACCM6 AMIP experiments are similar. Experiments with WACCM-SC (no chemistry) look similar to CESM2-WACCM6, indicating that chemical-climate interactions and aerosol differences are not the cause. However, in a WACCM6 experiment without convective gravity waves, high-latitude variability looks more like CESM2-CAM6, indicating that momentum forcing of the stratosphere is likely important.

Improvements in tropospheric variability can also be seen in a metric of atmospheric blocking. Figure 15 illustrates a longitudinal index of blocking defined as the frequency of the meridional gradient of 500-hPa geopotential height below a threshold (−5 m/degree) (D'Andrea et al., 1998). Figure 15 illustrates the blocking frequency from CESM1 (LENS, 35 simulations), CESM2-CAM (5 simulations), and CESM2-WACCM (3 simulations), all coupled to an active ocean. CESM2 is better at many locations than CESM1. March–May (MAM) is better than December–February (DJF) for all versions. In common with many CMIP5 models (Dunn-Sigouin & Son, 2013), CESM2 still has a DJF bias over the Atlantic, but there are significant improve-

Table 3
WACCM and CAM Simulation Global Averages Compared to Observations From Historical (AMIP) Simulations

Variable	Unit	WACCM6	WACCM4-CCMI	CAM6	Obs
AMIP Simulations FLNT					
	W/m^2	**237.4**	233.3	236.6	239.7
FSNT	W/m^2	241.0	235.0	**239.7**	240.5
FLNTC	W/m^2	262.1	**264.0**	260.3	265.7
FSNTC	W/m^2	**289.3**	291.5	**287.4**	287.6
SWCRE	W/m^2	**−48.4**	−56.5	**−47.7**	−47.1
LWCRE	W/m^2	**24.6**	30.8	23.7	26.1
CLDTOT	%	69.5	55.4	69.1	66.8
CLDHGH	%	44.1	33.0	43.6	40.3
CLDLOW	%	40.9	35.4	40.8	43.1
LWP	gm^{-2}	66.5	132.3	66.7	
IWP	gm^{-2}	13.4	16.3	12.8	
1850 Coupled Simulations					
		CESM2-WACCM6	CESM1-WACCM4	CESM2-CAM6	
Ts	K	288.0	287.6	288.2	
Precip	mm/day	2.93	2.92	2.83	
Global SIE	10^6 km^2	25.9	30.4	25.4	
NH SIE	10^6 km^2	11.5	14.0	11.2	
Global SIV	10^3 km^3	41.2		36.5	
NH SIV	10^3 km^3	26.2		21.8	

Note. Observations: CLDTOT (total cloud cover), CLDHGH (cloud cover for $p < 400$ hPa), CLDLOW (cloud cover for $p > 700$ hPa) from CLOUDSAT+CALIPSO joint data product. Fluxes are compared to CERES EBAF 2.4 (Loeb et al., 2009) for shortwave/longwave net at top of atmosphere for all sky (FSNT, FLNT) and clear sky (FSNTC, FNTC). Cloud radiative effects are the difference (LWCRE = FLNT − FLNTC and SWCRE = FSNT − FSNTC). Liquid and ice water path (LWP, IWP) do not have well constrained satellite estimates. For preindustrial (PI) 1,850 control simulations, variables are surface temperature (Ts), preciptiation rate (Precip), sea ice extent (SIE) and sea ice volume (SIV). **Bold** values are within the range of uncertainty of the observed values.

ments (outside of the ensemble spread from CESM1) in CESM2 near the Greenland blocking "bump" at 30°W in March–May, particularly in CESM2-WACCM6. CESM2-WACCM6 is also significantly better (outside of the ensemble spread) than CESM2-CAM6 in the Pacific sector during DJF. Note that the North Pacific is subject to much larger interannual variable than the Atlantic, because of stationary wave activity from the tropics.
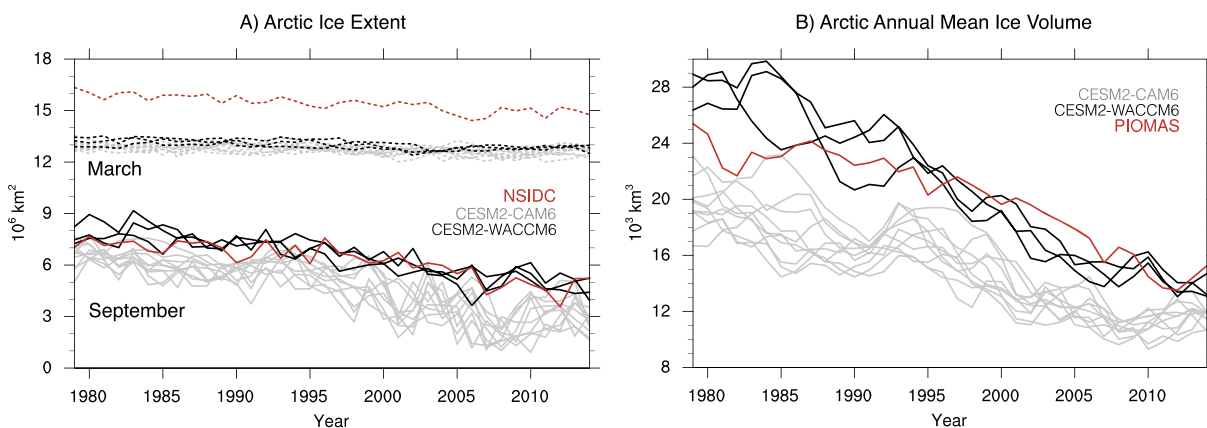

Figure 13. (a) Arctic sea ice extent in March (dashed) and September (solid). (b) Arctic annual mean sea ice volume. CESM2-WACCM6 (black), CESM2-CAM6 (gray). National Snow and Ice Data Center (NSIDC) ice extent satellite observations (red) (Fetterer et al., 2017) for (a) and Pan-Arctic Ice Ocean Modeling and Assimilation System (PIOMAS) ice volume estimate (red) (Schweiger et al., 2011) for (b).
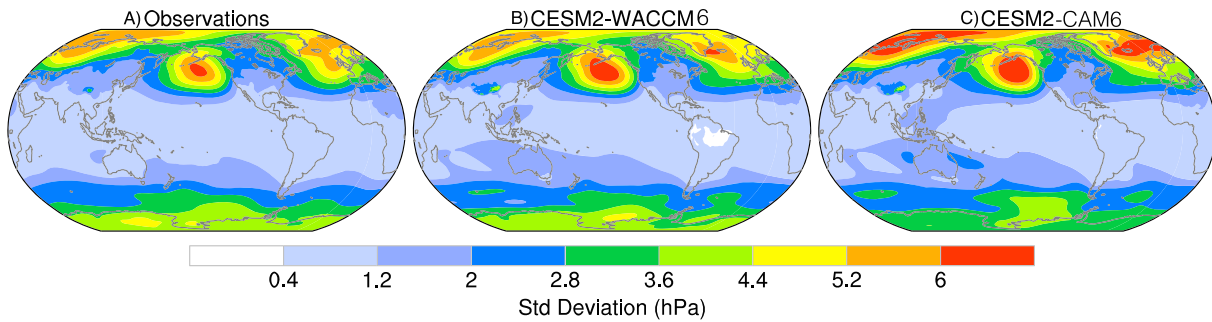
Figure 14. Interannual standard deviation of December–February averaged sea level pressure (hPa) from (a) ERA twentieth century reanalysis, (b) CESM2-WACCM6 coupled historical simulation ensemble member, and (c) CESM2-CAM6 coupled historical simulation ensemble member.

6.2. WACCM6 Versus WACCM4

Table 3 highlights several important differences in the climate of WACCM6 versus WACCM4. The tropospheric cloud radiative forcing (SWCRE and LWCRE) is lower and closer to observations (CERES-EBAF). WACCM6 has higher cloud fraction (closer to obs) with reduced LWP, which is also more in line with observations where available (global values are not available). These results are consistent with improvements in CAM6 over CAM4.

For preindustrial (1850) control climates, CESM2-WACCM6 has higher global mean precipitation, but very similar surface temperature (Table 3). The global sea ice extent in WACCM4 (Marsh et al., 2013) is 20% higher than CESM2-WACCM6 or CESM2-CAM6.

WACCM6 and WACCM4 do a good job of reproducing tropical tropopause temperatures, but WACCM6 has a warmer summer tropopause temperature and increased annual cycle amplitude, in better agreement with observations. WACCM4 (dashed lines in Figure 4a) has a faster tape recorder propagation speed in the midstratosphere for free running simulations than WACCM6 (solid lines in Figure 4a). WACCM6 does a good job of reproducing the speed of the tape recorder compared to observations, with some vertical shifts. However, WACCM6 has a 0.5 ppm positive bias in summer, depending on the simulation (a coupled case looks better than the fixed SST case in Figure 4).

As noted in discussion of Figure 5, WACCM6 has slightly higher frequency of occurrence of SSWs than WACCM4, due to more late winter (March) warmings when compared to Marsh et al. (2013), Figure3.
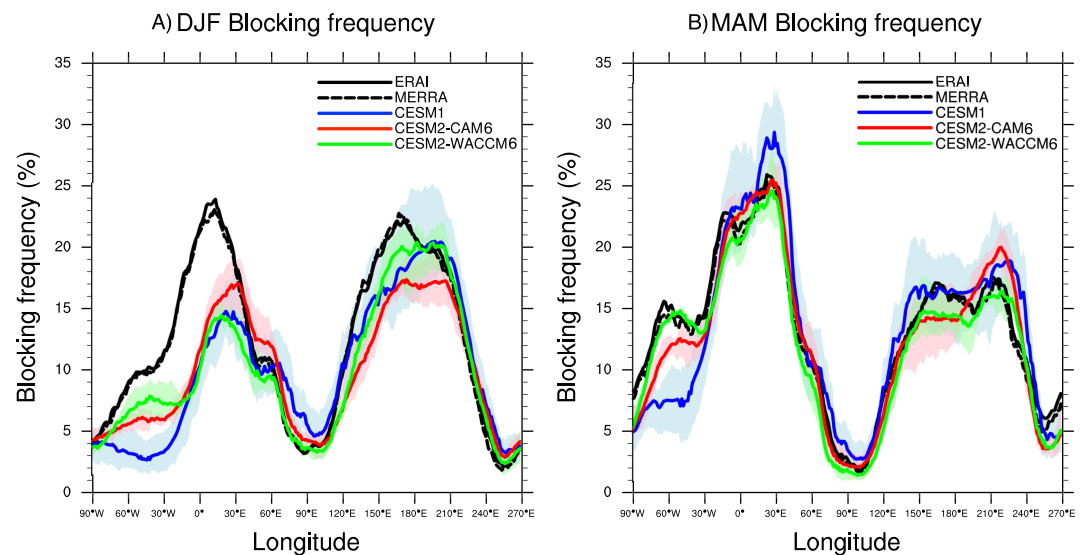

Figure 15. Northern Hemisphere blocking frequency defined following D'Andrea et al. (1998). Observations (black), CESM1 (blue), CESM2-CAM (red), and CESM2-WACCM (green) for (a) December–February (DJF) and (b) March–May (MAM). Averages are 1979–2005 from daily data and the shading is the full range of each ensemble set.

Finally, WACCM4 did not have an internally generated QBO, but it was forced to observations, while WACCM6 has an internally generated QBO (Figure 6).

7. Summary and Conclusions

WACCM6 represents the state of the art in simulation of the middle atmosphere up through the mesosphere. WACCM6 is available in several different configurations and can be run fully coupled in CESM2, with fixed SSTs (AMIP), or even with specified dynamics to produce observed dynamical variability. WACCM6 can also be run without full chemistry if just dynamical interactions are desired. WACCM-X (Liu et al., 2018) is a variant of WACCM that goes all the way to 500 km and represents additional thermosphere and ionospheric processes, with physical parameterizations for the lower atmosphere lagging one generation behind WACCM6.

WACCM6 is able to reproduce the observed climatology of temperatures, winds and trace constituents such as water vapor and ozone in the middle atmosphere. WACCM6 is able to reproduce stratospheric variability from SSWs, the response to volcanic eruptions, the QBO and long-term secular trends in the middle atmosphere. Biases in temperatures, winds, and water vapor are small, and smaller than previous versions of WACCM. Volcanic emissions are fully prognostic from gas phase through stratospheric aerosol, improving temperature response to volcanic eruptions. Despite temperature biases in spring and early summer in the Southern Hemisphere polar stratosphere, WACCM6 is able to reproduce the evolution of the 20th and 21st century ozone. There are some biases in the tropics likely due to the speed of tropical upwelling.

WACCM6 features exactly the same lower atmosphere physical parameterizations and horizontal resolution as CAM6, making it very useful for comparable studies of the model top, as well as the impact of chemistry/aerosols in the troposphere and stratosphere. CAM6 uses specified stratospheric aerosol from WACCM6, as it was found that without interactive oxidants (OH), the lifetime of stratospheric SO_2 under high loading was different (and not correct). The present day climate of WACCM6 is nearly identical to CAM6 global mean variables, with similar trends over the twentieth century in surface temperature. There are some differences due to absorption and scattering above the CAM6 top in WACCM6, and due to different evolution of tropospheric aerosols with the full tropospheric chemistry of WACCM6, that alters aerosol lifetime, particularly for organic aerosols. This can impact regional climate as well as sea ice. Thus, tropospheric chemistry and aerosols can significantly impact Arctic climate, improving sea ice extent and volume in CESM2-WACCM6 over CESM2-CAM6.

Finally, there are some indications that the stratosphere can improve climate variability, even at the surface. High-latitude variability in CESM2-WACCM6, in particular, the standard deviation of winter sea level pressure, is lower in CESM2-WACCM6 than in CESM2-CAM6, in better agreement with observations. This extends to WACCM-SC without chemistry and seems to be related to gravity wave momentum in CESM2-WACCM6. Blocking frequency is also closer to observed in CESM2-WACCM6 than CESM2-CAM6. This indicates that stratospheric dynamical processes are important for high-latitude tropospheric climate variability. Thus, stratospheric dynamics should be considered and resolved in studies of high-latitude climate variability.

References

Andersson, M. E., Verronen, P. T., Marsh, D. R., Päivärinta, S.-M., & Plane, J. M. C. (2016). WACCM-D—Improved modeling of nitric acid and active chlorine during energetic particle precipitation. *Journal of Geophysical Research: Atmospheres*, *121*, 10,328–10,341. https://doi.org/10.1002/2015JD024173

Ansmann, A., Mattis, I., Wandinger, U., Wagner, F., Reichardt, J., & Deshler, T. (1997). Evolution of the Pinatubo Aerosol: Raman Lidar Observations of Particle Optical Depth, Effective Radius, Mass, and Surface Area over Central Europe at 53.4N. *Journal of the Atmospheric Sciences*, *54*(22), 2630–2641. https://doi.org/10.1175/1520-0469(1997)054<2630:EOTPAR>2.0.CO;2

Ayarzagüena, B., Palmeiro, F. M., Barriopedro, D., Calvo, N., Langematz, U., & Shibata, K. (2019). On the representation of major stratospheric warmings in reanalyses. *Atmospheric Chemistry and Physics*, *19*, 9469–9484. https://doi.org/10.5194/acp-19-9469-2019

Bacmeister, J. T., Newman, P. A., Gary, B. L., & Chan, K. R. (1994). An Algorithm for Forecasting Mountain Wave–Related Turbulence in the Stratosphere. *Weather and Forecasting*, *9*(2), 241–253. https://doi.org/10.1175/1520-0434(1994)009<0241:AAFFMW>2.0.CO;2

Baldwin, M. P., & Dunkerton, T. J. (2001). Stratospheric Harbingers of Anomalous weather Regimes. *Science*, *294*, 581–584.

Beljaars, A. C. M., Brown, A. R., & Wood, N. (2004). A new parametrization of turbulent orographic form drag. *Quarterly Journal of the Royal Meteorological Society*, *130*(599), 1327–1347. https://doi.org/10.1256/qj.03.73

Bogenschutz, P. A., Gettelman, A., Morrison, H., Larson, V. E., Craig, C., & Schanen, D. P. (2013). Higher-order turbulence closure and its impact on Climate Simulation in the Community Atmosphere Model. *Journal of Climate*, *26*(23), 9655–9676. https://doi.org/10.1175/JCLI-D-13-00075.1

Boville, B. A., Rasch, P. J., Hack, J. J., & McCaa, J. R. (2006). Represenation of Clouds and Precipitation in the Community Atmosphere Model Version 3 (CAM3). *Journal of Climate*, *19*(11), 2184–2198.

Brasseur, G. P., & Solomon, S. (1986). In D. Reidel (Ed.), *Aeronomy of the Middle Atmosphere* (2nd ed.). Norwell, Mass: Springer.

Burkholder, J. B., Sander, S. P., Abbatt, J. P. D., Barker, J. R., Huie, R. E., Kolb, C. E., et al. (2015). Chemical kinetics and photochemical data for use in atmospheric studies: Evaluation number 18, *Technical Report*, Pasadena, CA: Jet Propulsion Laboratory, National Aeronautics and Space Administration, 2015.

Butchart, N., Charlton-Perez, A. J., Cionni, I., Hardiman, S. C., Haynes, P. H., Krüger, K., et al. (2011). Multimodel climate and variability of the stratosphere. *Journal of Geophysical Research*, *116*, D05102. https://doi.org/10.1029/2010JD014995

Calvo, N., Garcia, R. R., Randel, W. J., & Marsh, D. R. (2010). Dynamical Mechanism for the Increase in Tropical Upwelling in the Lowermost Tropical Stratosphere during Warm ENSO Events. *Journal of the Atmospheric Sciences*, *67*(7), 2331–2340. https://doi.org/10.1175/2010JAS3433.1

Charlton, A. J., & Polvani, L. M. (2007). A New Look at Stratospheric Sudden Warmings. Part I: Climatology and Modeling Benchmarks. *Journal of Climate*, *20*(3), 449–469. https://doi.org/10.1175/JCLI3996.1

Charlton-Perez, A. J., Baldwin, M. P., Birner, T., Black, R. X., Butler, A. H., Calvo, N., et al. (2013). On the lack of stratospheric dynamical variability in low-top versions of the CMIP5 models. *Journal of Geophysical Research: Atmospheres*, *118*, 2494–2505. https://doi.org/10.1002/jgrd.50125

Coddington, O., Lean, J. L., Pilewskie, P., Snow, M., & Lindholm, D. (2015). A Solar Irradiance Climate Data Record. *Bulletin of the American Meteorological Society*, *97*(7), 1265–1282. https://doi.org/10.1175/BAMS-D-14-00265.1

Collins, W. D., Hackney, J. K., & Edwards, D. P. (2002). An updated parameterization for infrared emission and absorption by water vapor in the National Center for Atmospheric Research Community Atmosphere Model. *Journal of Geophysical Research*, *107*(D22), 4664. https://doi.org/10.1029/2001JD001365

Cowtan, K., & Way, R. G. (2014). Coverage bias in the HadCRUT4 temperature series and its impact on recent temperature trends. *Quarterly Journal of the Royal Meteorological Society*, *140*(682), 1935–1944. https://doi.org/10.1002/qj.2297

D'Andrea, F., Tibaldi, S., Blackburn, M., Boer, G., Déqué, M., Dix, M. R., et al. (1998). Northern Hemisphere atmospheric blocking as simulated by 15 atmospheric general circulation models in the period 1979–1988. *Climate Dynamics*, *14*(6), 385–407. https://doi.org/10.1007/s003820050230

de la Torre, L., Garcia, R. R., Barriopedro, D., & Chandran, A. (2012). Climatology and characteristics of stratospheric sudden warmings in the Whole Atmosphere Community Climate Model. *Journal of Geophysical Research*, *117*, D04110. https://doi.org/10.1029/2011JD016840

Dunn-Sigouin, E., & Son, S.-W. (2013). Northern Hemisphere blocking frequency and duration in the CMIP5 models. *Journal of Geophysical Research: Atmospheres*, *118*(3), 1179–1188. https://doi.org/10.1002/jgrd.50143

Emmons, L. K., Walters, S., Hess, P. G., Lamarque, J.-F., Pfister, G. G., Fillmore, D., et al. (2010). Description and evaluation of the Model for Ozone and Related chemical Tracers, version 4 (MOZART-4). *Geoscientific Model Development*, *3*(1), 43–67. https://doi.org/10.5194/gmd-3-43-2010

Eyring, V., Bony, S., Meehl, G. A., Senior, C. A., Stevens, B., Stouffer, R. J., & Taylor, K. E. (2016). Overview of the Coupled Model Intercomparison Project Phase 6 (CMIP6) experimental design and organization. *Geoscientific Model Development*, *9*(5), 1937–1958. https://doi.org/10.5194/gmd-9-1937-2016

Eyring, V., et al. (2007). Multi-model projections of stratospheric ozone in the 21st century. *Journal of Geophysical Research*, *112*, D16303. https://doi.org/10.1029/2006JD008332

Eyring, V., et al. (2010). Sensitivity of 21st century stratospheric ozone to greenhouse gas scenarios. *Geophysical Research Letters*, *37*, L16807. https://doi.org/10.1029/2010GL044443

Fetterer, F., Knowles, K., Meier, W. N., Savoie, M. , & Windnagel, A. K. (2017). Sea Ice Index, Version 3, https://doi.org/10.7265/n5k072f8.

Garcia, R. R., Marsh, D., Kinnison, D., Boville, B. A., & Sassi, F. (2007). Simulations of secular trends in the middle atmosphere, 1950-2003. *Journal of Geophysical Research*, *112*, D09301. https://doi.org/10.1029/2006JD007485

Garcia, R. R., & Richter, J. H. (2018). On the Momentum Budget of the Quasi-Biennial Oscillation in the Whole Atmosphere Community Climate Model. *Journal of the Atmospheric Sciences*, *76*(1), 69–87. https://doi.org/10.1175/JAS-D-18-0088.1

Gettelman, A., & Birner, T. (2007). Insights on Tropical Tropopause Layer Processes using Global Models. *Journal of Geophysical Research*, *112*, D23104. https://doi.org/10.1029/2007JD008945

Gettelman, A., & Morrison, H. (2015). Advanced Two-Moment Bulk Microphysics for Global Models. Part I: Off-Line Tests and Comparison with Other Schemes. *Journal of Climate*, *28*(3), 1268–1287. https://doi.org/10.1175/JCLI-D-14-00102.1

Guenther, A. B., Jiang, X., Heald, C. L., Sakulyanontvittaya, T., Duhl, T., Emmons, L. K., & Wang, X. (2012). The Model of Emissions of Gases and Aerosols from Nature version 2.1 (MEGAN2.1): An extended and updated framework for modeling biogenic emissions. *Geoscientific Model Development*, *5*(6), 1471–1492. https://doi.org/10.5194/gmd-5-1471-2012

Hack, J. J. (1994). Parameterization of moist convection in the National Center for Atmospheric Research community climate model (CCM2). *Journal of Geophysical Research*, *99*(D3), 5551–5568. https://doi.org/10.1029/93JD03478

Hansen, J., Ruedy, R., Sato, M., & Lo, K. (2010). Global surface temperature change. *Reviews of Geophysics*, *48*, RG4004. https://doi.org/10.1029/2010RG000345

Heald, C. L., Henze, D. K., Horowitz, L. W., Feddema, J., Lamarque, J.-F., Guenther, A., et al. (2008). Predicted change in global secondary organic aerosol concentrations in response to future climate, emissions, and land use change. *Journal of Geophysical Research*, *113*, D05211. https://doi.org/10.1029/2007JD009092

Hodzic, A., Kasibhatla, P. S., Jo, D. S., Cappa, C. D., Jimenez, J. L., Madronich, S., & Park, R. J. (2016). Rethinking the global secondary organic aerosol (SOA) budget: Stronger production, faster removal, shorter lifetime. *Atmospheric Chemistry and Physics*, *16*(12), 7917–7941. https://doi.org/10.5194/acp-16-7917-2016

Hodzic, A., & Madronich, S. (2018). Response of surface ozone over the continental United States to UV radiation declines from the expected recovery of stratospheric ozone. *npj Climate and Atmospheric Science*, *1*(1), 35. https://doi.org/10.1038/s41612-018-0045-5

Hodzic, A., Madronich, S., Kasibhatla, P. S., Tyndall, G., Aumont, B., Jimenez, J. L., et al. (2015). Organic photolysis reactions in tropospheric aerosols: Effect on secondary organic aerosol formation and lifetime. *Atmospheric Chemistry and Physics*, *15*(16), 9253–9269. https://doi.org/10.5194/acp-15-9253-2015

Hoesly, R. M., Smith, S. J., Feng, L., Klimont, Z., Janssens-Maenhout, G., Pitkanen, T., et al. (2018). Historical (1750–2014) anthropogenic emissions of reactive gases and aerosols from the Community Emissions Data System (CEDS). *Geoscientific Model Development*, *11*(1), 369–408. https://doi.org/10.5194/gmd-11-369-2018

Hofmann, D., Barnes, J., O'Neill, M., Trudeau, M., & Neely, R. (2009). Increase in background stratospheric aerosol observed with lidar at Mauna Loa Observatory and Boulder, Colorado. *Geophysical Research Letters*, *36*, L15808. https://doi.org/10.1029/2009GL039008

Iacono, M. J., Delamere, J. S., Mlawer, E. J., Shephard, M. W., Clough, S. A., & Collins, W. D. (2008). Radiative forcing by long-lived greenhouse gases: Calculations with the AER radiative transfer models. *Journal of Geophysical Research*, *113*, D13103. https://doi.org/10.1029/2008JD009944

Jackman, C. H., Marsh, D. R., Vitt, F. M., Garcia, R. R., Randall, C. E., Fleming, E. L., & Frith, S. M. (2009). Long-term middle atmospheric influence of very large solar proton events. *Journal of Geophysical Research*, *114*, D11304. https://doi.org/10.1029/2008JD011415

Kinnison, D. E., et al. (2007). Sensitivity of Chemical Tracers to Meteorological Parameters in the MOZART-3 Chemical Transport Model. *Journal of Geophysical Research*, *112*, D20302. https://doi.org/10.1029/2006JD007879

Knote, C., Hodzic, A., Jimenez, J. L., Volkamer, R., Orlando, J. J., Baidar, S., et al. (2014). Simulation of semi-explicit mechanisms of SOA formation from glyoxal in aerosol in a 3-D model. *Atmospheric Chemistry and Physics*, *14*(12), 6213–6239. https://doi.org/10.5194/acp-14-6213-2014

Lamarque, J.-F., Emmons, L. K., Hess, P. G., Kinnison, D. E., Tilmes, S., Vitt, F., et al. (2012). CAM-chem: Description and evaluation of interactive atmospheric chemistry in the Community Earth System Model. *Geoscientific Model Development*, *5*(2), 369–411. https://doi.org/10.5194/gmd-5-369-2012

Larson, V. E., Golaz, J.-C., & Cotton, W. R. (2002). Small-Scale and Mesoscale Variability in Cloudy Boundary Layers: Joint Probability Density Functions. *Journal of the Atmospheric Sciences*, *59*(24), 3519–3539. https://doi.org/10.1175/1520-0469(2002)059<3519:SSAMVI>2.0.CO;2

Lefohn, A. S., Malley, C. S., Smith, L., Wells, B., Hazucha, M., Simon, H., et al. (2018). Tropospheric ozone assessment report: Global ozone metrics for climate change, human health, and crop/ecosystem research. *Elementa: Science of the Anthropocene*, *6*(1), 28. https://doi.org/10.1525/elementa.279

Lin, S. J., & Rood, R. B. (1997). An explicit Flux-Form Semi-Lagrangian shallow water model on the sphere. *Quarterly Journal of the Royal Meteorological Society*, *123*, 2477–2498.

Liu, J., Liu, H., Wang, W., Burns, A. G., Wu, Q., Gan, Q., et al. (2018). First Results From the Ionospheric Extension of WACCM-X During the Deep Solar Minimum Year of 2008. *Journal of Geophysical Research: Space Physics*, *123*, 1534–1553. https://doi.org/10.1002/2017JA025010

Liu, X., Easter, R. C., Ghan, S. J., Zaveri, R., Rasch, P., Shi, X., et al. (2012). Toward a minimal representation of aerosols in climate models: Description and evaluation in the Community Atmosphere Model CAM5. *Geoscientific Model Development*, *5*(3), 709–739. https://doi.org/10.5194/gmd-5-709-2012

Liu, X., Ma, P.-L., Wang, H., Tilmes, S., Singh, B., Easter, R. C., et al. (2016). Description and evaluation of a new four-mode version of the Modal Aerosol Module (MAM4) within version 5.3 of the Community Atmosphere Model. *Geoscientific Model Development*, *9*(2), 505–522. https://doi.org/10.5194/gmd-9-505-2016

Loeb, N. G., Wielicki, B. A., Doelling, D. R., Smith, G. L., Keyes, D. F., Kato, S., et al. (2009). Towards Optimal Closure of the Earth's Top-of-Atmosphere Radiation Budget. *The Journal of Commerce*, *22*, 748–766. https://doi.org/10.1175/2008JCLI2637.1

Marsh, D. R., Garcia, R. R., Kinnison, D. E., Boville, B. A., Sassi, F., Solomon, S. C., & Matthes, K. (2007). Modeling the whole atmosphere response to solar cycle changes in radiative and geomagnetic forcing. *Journal of Geophysical Research*, *112*, D23306. https://doi.org/10.1029/2006JD008306

Marsh, D. R., Mills, M. J., Kinnison, D. E., Lamarque, J.-F., Calvo, N., & Polvani, L. M. (2013). Climate Change from 1850 to 2005 Simulated in CESM1(WACCM). *Journal of Climate*, *26*(19), 7372–7391. https://doi.org/10.1175/JCLI-D-12-00558.1

Matthes, K., Funke, B., Andersson, M. E., Barnard, L., Beer, J., Charbonneau, P., et al. (2017). Solar forcing for CMIP6 (v3.2). *Geoscientific Model Development*, *10*(6), 2247–2302. https://doi.org/10.5194/gmd-10-2247-2017

Matthes, K., Marsh, D. R., Garcia, R. R., Kinnison, D. E., Sassi, F., & Walters, S. (2010). Role of the QBO in modulating the influence of the 11 year solar cycle on the atmosphere using constant forcings. *Journal of Geophysical Research*, *115*, D18110. https://doi.org/10.1029/2009JD013020

McTurf, R. M. (1978). Stratospheric warmings: Synoptic, dynamic and general-circulation aspects.

Meinshausen, M., Smith, S. J., Calvin, K., Daniel, J. S., Kainuma, M. L. T., Lamarque, J.-F., et al. (2011). The RCP greenhouse gas concentrations and their extensions from 1765 to 2300. *Climatic Change*, *109*(1), 213. https://doi.org/10.1007/s10584-011-0156-z

Meinshausen, M., Vogel, E., Nauels, A., Lorbacher, K., Meinshausen, N., Etheridge, D. M., et al. (2017). Historical greenhouse gas concentrations for climate modelling (CMIP6). *Geoscientific Model Development*, *10*(5), 2057–2116. https://doi.org/10.5194/gmd-10-2057-2017

Mills, M. J., Richter, J. H., Tilmes, S., Kravitz, B., MacMartin, D. G., Glanville, A. A., et al. (2017). Radiative and Chemical Response to Interactive Stratospheric Sulfate Aerosols in Fully Coupled CESM1(WACCM). *Journal of Geophysical Research: Atmospheres*, *122*, 13,061–13,078. https://doi.org/10.1002/2017JD027006

Mills, M. J., Schmidt, A., Easter, R., Solomon, S., Kinnison, D. E., Ghan, S. J., et al. (2016). Global volcanic aerosol properties derived from emissions, 1990–2014, using CESM1(WACCM). *Journal of Geophysical Research: Atmospheres*, *121*, 2332–2348. https://doi.org/10.1002/2015JD024290

Mlawer, E. J., Taubman, S. J., Brown, P. D., Iacono, M. J., & Clough, S. A. (1997). Radiative transfer for inhomogeneous atmospheres: RRTM, a validated correlated-k model for the longwave. *Journal of Geophysical Research*, *102*(D14), 16,663–16,682. https://doi.org/10.1029/97JD00237

Molod, A., Takacs, L., Suarez, M., & Bacmeister, J. (2015). Development of the GEOS-5 atmospheric general circulation model: Evolution from MERRA to MERRA2. *Geoscientific Model Development*, *8*(5), 1339–1356. https://doi.org/10.5194/gmd-8-1339-2015

Montzka, S. A., Aydin, M., Battle, M., Butler, J. H., Saltzman, E. S., Hall, B. D., et al. (2004). A 350-year atmospheric history for carbonyl sulfide inferred from Antarctic firn air and air trapped in ice. *Journal of Geophysical Research*, *109*, D22302. https://doi.org/10.1029/2004JD004686

Mote, P. W., Rosenlof, K. H., McIntyre, M. E., Carr, E. S., Gille, J. C., Holton, J. R., et al. (1996). An atmospheric tape recorder: The imprint of tropical tropopause temperatures on stratospheric water vapor. *Journal of Geophysical Research*, *101*(D2), 3989–4006.

Neale, R. B., Chen, C. C., Gettelman, A., Lauritzen, P. H., Park, S., Williamson, D. L., et al. (2010), Description of the NCAR Community Atmosphere Model (CAM5.0), Tech. Rep. NCAR/TN-486+STR, National Center for Atmospheric Research, Boulder, CO, USA.

Neale, R. B., Richter, J. H., & Jochum, M. (2008). The Impact of Convection on ENSO: From a Delayed Oscillator to a Series of Events. *Journal of Climate*, 21, 5904. https://doi.org/10.1175/2008JCLI2244.1

Neely, R. R., & Schmidt, A. (2016). VolcanEESM: Global volcanic sulphur dioxide (SO2) emissions database from 1850 to present - Version 1.0, https://doi.org/10.5285/76ebdc0b-0eed-4f70-b89e-55e606bcd568.

Orsolini, Y. J., Smith-Johnsen, C., Marsh, D. R., Stordal, F., Rodger, C. J., Verronen, P. T., & Clilverd, M. A. (2018). Mesospheric Nitric Acid Enhancements During Energetic Electron Precipitation Events Simulated by WACCM-D. *Journal of Geophysical Research: Atmospheres*, *123*, 6984–6998. https://doi.org/10.1029/2017JD028211

Park, S., & Bretherton, C. S. (2009). The University of Washington shallow convection and moist turbulence schemes and their impact on climate simulations with the Community Atmosphere Model. *Journal of Climate*, *22*, 3449–3469.

Park, S., Bretherton, C. S., & Rasch, P. J. (2014). Integrating Cloud Processes in the Community Atmosphere Model, Version 5. *Journal of Climate*, *27*(18), 6821–6856. https://doi.org/10.1175/JCLI-D-14-00087.1

Randel, W. J., Polvani, L., Wu, F., Kinnison, D. E., Zou, C.-Z., & Mears, C. (2017). Troposphere-Stratosphere Temperature Trends Derived From Satellite Data Compared With Ensemble Simulations From WACCM. *Journal of Geophysical Research: Atmospheres*, *122*, 9651–9667. https://doi.org/10.1002/2017JD027158

Read, W. G., et al. (2007). Aura Microwave Limb Sounder upper tropospheric and lower stratospheric H_2O and relative humidity with respect to ice validation. *Journal of Geophysical Research*, *112*, D24S35. https://doi.org/10.1029/2007JD008752

Richter, J. H., Sassi, F., & Garcia, R. R. (2010). Toward a Physically Based Gravity Wave Source Parameterization in a General Circulation Model. *Journal of the Atmospheric Sciences*, *67*(1), 136–156. https://doi.org/10.1175/2009JAS3112.1

Ridley, D. A., Solomon, S., Barnes, J. E., Burlakov, V. D., Deshler, T., Dolgii, S. I., et al. (2014). Total volcanic stratospheric aerosol optical depths and implications for global climate change. *Geophysical Research Letters*, *41*, 7763–7769. https://doi.org/10.1002/2014GL061541

Rienecker, M. M., et al. (2011). MERRA: NASA's modern-era retrospective analysis for research and applications. *The Journal of Commerce*, *24*, 3624–3648. https://doi.org/10.1175/JCLI-D-11-00015.1

Roble, R. G., & Ridley, E. C. (1994). A thermosphere-ionosphere-mesosphere-electrodynamics general circulation model (time-GCM): Equinox solar cycle minimum simulations (30–500 km). *Geophysical Research Letters*, *21*(6), 417–420. https://doi.org/10.1029/93GL03391

Sakai, T., Uchino, O., Nagai, T., Liley, B., Morino, I., & Fujimoto, T. (2016). Long-term variation of stratospheric aerosols observed with lidars over Tsukuba, Japan, from 1982 and Lauder, New Zealand, from 1992 to 2015. *Journal of Geophysical Research: Atmospheres*, *121*, 10,283–10,293. https://doi.org/10.1002/2016JD025132

Sassi, F., Kinnison, D., Boville, B. A., Garcia, R. R., & Roble, R. (2004). The Effect of ENSO on the Dynamical, Thermal and Chemical Structure of the Middle Atmosphere. *Journal of Geophysical Research*, *109*, D17108. https://doi.org/10.1029/2003JD004434

Schweiger, A., Lindsay, R., Zhang, J., Steele, M., Stern, H., & Kwok, R. (2011). Uncertainty in modeled Arctic sea ice volume. *Journal of Geophysical Research*, *116*, C00D06. https://doi.org/10.1029/2011JC007084

Scinocca, J. F., & McFarlane, N. A. (2000). The parametrization of drag induced by stratified flow over anisotropic orography. *Quarterly Journal of the Royal Meteorological Society*, *126*(568), 2353–2393. https://doi.org/10.1002/qj.49712656802

Smith, A. K., Garcia, R. R., Moss, A. C., & Mitchell, N. J. (2017). The Semiannual Oscillation of the Tropical Zonal Wind in the Middle Atmosphere Derived from Satellite Geopotential Height Retrievals. *Journal of the Atmospheric Sciences*, *74*(8), 2413–2425. https://doi.org/10.1175/JAS-D-17-0067.1

Smith, K. L., Neely, R. R., Marsh, D. R., & Polvani, L. M. (2014). The Specified Chemistry Whole Atmosphere Community Climate Model (SC-WACCM). *Journal of Advances in Modeling Earth Systems*, *6*, 883–901. https://doi.org/10.1002/2014MS000346

Solomon, S., Kinnison, D., Bandoro, J., & Garcia, R. (2015). Simulation of polar ozone depletion: An update. *Journal of Geophysical Research-Atmospheres*, *120*, 7958–7974. https://doi.org/10.1002/2015JD023365

Solomon, S., Rosenlof, K. H., Portmann, R. W., Daniel, J. S., Davis, S. M., Sanford, T. J., & Plattner, G.-K. (2010). Contributions of Stratospheric Water Vapor to Decadal Changes in the Rate of Global Warming. *Science*, *327*(5970), 1219–1223. https://doi.org/10.1126/science.1182488

Solomon, S. C., & Qian, L. (2005). Solar extreme-ultraviolet irradiance for general circulation models. *Journal of Geophysical Research*, *110*, A10306. https://doi.org/10.1029/2005JA011160

Son, S. W., et al. (2010). Impact of stratospheric ozone on Southern Hemisphere circulation change: A multimodel assessment. *Journal of Geophysical Research*, *115*, D00M07. https://doi.org/10.1029/2010JD014271

Tabazadeh, A., Turco, R. P., & Jacobson, M. Z. (1994). A model for studying the composition and chemical effects of stratospheric aerosols. *Journal of Geophysical Research*, *99*(D6), 12,897–12,914. https://doi.org/10.1029/94JD00820

Thompson, D. W. J., Baldwin, M. P., & Wallace, J. M. (2002). Stratospheric Connection to Northern Hemisphere Wintertime Weather: Implications for Prediction. *Journal of Climate*, *15*(12), 1421–1428. https://doi.org/10.1175/1520-0442(2002)015<1421:SCTNHW>2.0.CO;2

Tilmes, S., Garcia, R. R., Kinnison, D. E., Gettelman, A., & Rasch, P. J. (2009). Impact of geoengineered aerosols on the troposphere and stratosphere. *Journal of Geophysical Research*, *114*, D12305. https://doi.org/10.1029/2008JD011420

Tilmes, S., Lamarque, J.-F., Emmons, L. K., Kinnison, D. E., Marsh, D., Garcia, R. R., et al. (2016). Representation of the Community Earth System Model (CESM1) CAM4-chem within the Chemistry-Climate Model Initiative (CCMI). *Geoscientific Model Development*, *9*(5), 1853–1890. https://doi.org/10.5194/gmd-9-1853-2016

de la Torre, L., Garcia, R. R., Barriopedro, D., & Chandran, A. (2012). Climatology and characteristics of stratospheric sudden warmings in the Whole Atmosphere Community Climate Model. *Journal of Geophysical Research*, *117*, D04110. https://doi.org/10.1029/2011JD016840

vanMarle, M. J. E., Kloster, S., Magi, B. I., Marlon, J. R., Daniau, A.-L., Field, R. D., et al. (2017). Historic global biomass burning emissions for CMIP6 (BB4CMIP) based on merging satellite observations with proxies and fire models (1750–2015). *Geoscientific Model Development*, *10*(9), 3329–3357. https://doi.org/10.5194/gmd-10-3329-2017

Verronen, P. T., Andersson, M. E., Marsh, D. R., Kovács, T., & Plane, J. M. C. (2016). WACCM-D—Whole Atmosphere Community Climate Model with D-region ion chemistry. *Journal of Advances in Modeling Earth Systems*, *8*, 954–975. https://doi.org/10.1002/2015MS000592

Waters, J. W., et al. (2006). The Earth Observing System Microwave Limb Sounder (EOS MLS) on the Aura Satellite. *IEEE Transactions on Geoscience and Remote Sensing*, *44*, 1075–1092. https://doi.org/10.1109/TGRS.2006.873771

World Meteorological Organization (WMO) (2011). Scientific Assessment of Ozone Depletion: 2010, Global Ozone Research and Monitoring Project-Report No. 52, 516 pp., Geneva, Switzerland.

Yeo, K. L., Ball, W. T., Krivova, N. A., Solanki, S. K., Unruh, Y. C., & Morrill, J. (2015). UV solar irradiance in observations and the NRLSSI and SATIRE-S models. *Journal of Geophysical Research: Space Physics*, *120*, 6055–6070. https://doi.org/10.1002/2015JA021277

Zhang, G. J., & McFarlane, N. A. (1995). Sensitivity of climate simulations to the parameterization of cumulus convection in the Canadian Climate Center general circulation model. *Atmosphere-Ocean*, *33*, 407–446.

Zuev, V. V., Burlakov, V. D., Nevzorov, A. V., Pravdin, V. L., Savelieva, E. S., & Gerasimov, V. V. (2017). 30-year lidar observations of the stratospheric aerosol layer state over Tomsk (Western Siberia, Russia). *Atmospheric Chemistry and Physics*, *17*(4), 3067–3081. https://doi.org/10.5194/acp-17-3067-2017